이학박사 학위논문

Study on Electrical Detection and Control of Magnetic Domain Walls

자구벽의 전기적 감지와 제어에 대한 연구

2023 년 2 월

서울대학교 대학원

물리천문학부

이 성 협

Study on Electrical Detection and Control of Magnetic Domain Walls

자구벽의 전기적 감지와 제어에 대한 연구

지도 교수 최 석 봉

이 논문을 이학박사 학위논문으로 제출함
2023 년 2 월

서울대학교 대학원
물리천문학부
이 성 협

이성협의 이학박사 학위논문을 인준함
2023 년 2 월

위 원 장 ______ 장 준 호 ______ (인)

부위원장 ______ 최 석 봉 ______ (인)

위 원 ______ 김 도 헌 ______ (인)

위 원 ______ 이 탁 희 ______ (인)

위 원 ______ 정 종 율 ______ (인)

Study on Electrical Detection and Control of Magnetic Domain Walls

Seong-Hyub Lee

Supervised by
Professor Sug-Bong Choe

A Dissertation in Physics

Submitted to the Faculties of
Seoul National University
in partial Fulfillment of the Requirements for the Degree of
Doctor of Philosophy

February 2023

Department of Physics and Astronomy
The Graduate College of Natural Sciences
Seoul National University

Abstract

Metallic ferromagnetic film with perpendicular magnetic anisotropy (PMA) has long been highlighted by its utility in memory applications. Because of its high anisotropy, not only the thermal stability of magnetic domains can be easily achieved but also capacity of magnetic domains is made more densely. Because PMA in magnetic thin film structure is very sensitive to the thickness of ferromagnetic layer which is order of sub-nanometer and interface to the adjacent metal layer. As a result, we need for pure environment and well-controlled thickness of deposition. Within these PMA system, electrical response of magnetic domain walls (DWs) has long been studied for its fruitful underlying physical mechanisms and needs for next-generation memory applications. Especially, detecting and controlling the magnetic domain wall through electrical charge current is important for transferring magnetic domain to read the status of local magnetization which is binary state.

For the electrical detecting mechanism of magnetic domain walls, anomalous Hall effect (AHE) has been provieded and used in determining the direction of magnetization.

For the electrical control of magnetic domain walls, efforts to shed light on the physical mechanism has proposed the key parameters to efficiently control the DWs. One is spin-orbit torque (SOT) which is the main source pushing DWs via electric current. The other is Dzyaloshinskii-Moriya interaction (DMI), which makes the

DW as chiral Neel wall. These parameters which are originating from spin-orbit coupling are mainly generated from the heavy metal layer or heavy metal/ ferromagnetic metal interface in metallic multilayer system. As their mechanisms are shared, it is not easy to achieve the efficient current-induced domain wall motion by regulating these two key parameters independently.

After we find how to control these parameters independently, we focus on the precise control of magnetic domain walls. To use magnetic DWs as a data bit, there is problem which is the randomness of DWs. Because of randomly distributed pinning sites in ferromagnetic film, DWs shows stochastic travel distance with respect to the injected driving force. To control the random positionning problem of DWs, a number of studies has been reported, which include 2-dimensional geometrical constraints. However, using geometric notch can invoke the damage to the device edge and also needs for high current density.

Chapter 2 describes on the development of sputtering system to control the thickness of ferromagnetic layer within sub-monolayer thickness resolution. Computer-controlled shutter switch with real-time quartz crystal monitor system was setup. By using polar magneto-optical Kerr effect microscopy, we compared the deposited magnetic thin film's dynamic property of domain walls, which shows the resonable reproducibility maintained during a long period.

Chapter 3 focuses on the electrical detection of magnetic domain walls via anomalous Hall effect. The empirical relation between Hall voltage and domain wall position was derived through the three different kinds of analyses. Firstly, we observe that the Hall signal of magnetic domain wall can be detected outside the Hall bar. With the various combination of wire width and Hall bar width was experimentally analysed. After then to find relation between geometric parameters and detection range through a number of sets of combination, a numerical simulation was implemented. Finally, we modify the analytical equation to apply our experimental situation. With all the coincidence of different kinds of approaches, empirical relation was suggested.

Chapter 4 discusses about the electrical control of magnetic domain walls. From the exploration of diverse sample structures, here we provide the strategy to control the spin-orbit torque. Though controlling the spin-orbit torque was hard by changing the structure of trilayer, it was possible to solely control the spin-orbit torque by chaning the thickness of material. With this, the effective field of DMI didn't show any evident variation.

Chapter 5 studied on the position control of DWs, based on the result of chapter 4. From the result of prior chapter and the idea of H.-S. Whang, here we provide the way to pin the DWs at SOT-modulation boundary, and depin the DWs only in unidirection. DW pinning at the SOT-MB was firstly observed by using our P-MOKE microscope. After achieving the pinning at the SOT-MB we made the asymetric design of SOT-MD to make the DWs prefer unidirection motion.

Chapter 6 experimentally proves that SOT-modulation boundary mechanism can be used for the precise position control to the nano-sized device, which is the world record of control resolution.

With all the result describes above, here we provide a new strategy to control the magnetic domain wall only by using electric charge current.

Keyword : Perpendicular Magnetic Anisotropy**,** Domain Walls, Anomalous Hall effect, Spin-Orbit Torque, Dzyaloshinskii-Moriya interaction, Spin-Orbit Torque Modulation
Student number : 2017-21690

Contents

List of Figures

List of Tables

Chapter 1. Introduction

From the early days of 21th centry, the new area of research “spintronincs” arised. This research area makes use of the spin degree of freedom, in addition to the conventional electric circuit. Because of this new degree of freedom is intrinsic, a lot of physical phenomena and expectations for the next-generation memory boost the growth of this area. The needs for the fast processing speed of memory was increased to match the quantity of information. As the advent of complex information networks which include internet of things, autonomous driving and so on, a lot of memory shoud be fastly proccessed. And the conventional memory devices including Hard disk drive and random access memory meet the limit in its functionality.

As a candidate which accepts these abilities magnetic domain wall memory, also called as Racetrack memory, was suggested. With the low cost of data per bit in HDD, fast process speed is the merit of domain wall memory. However, there has been a vigorous debate about the electrical driving mechanism of the magnetic domain wall, which is confusing for the direction of DWs relative to the current. Even after spin-orbit torque was found to be the main mechanism of current-induced domain wall motion, there was debate on the underlying physical mechanism. In addition to this, Dzyaloshinskii-Moriya interaction also relevent for the efficiecny of CIDWM.

In this chapter, here we describe our base ferromagnetic system from perpendicular magnetic anisotropy to mechanism of CIDWM, which is the background information for the whole chapter.

1.1 Magnetic Anisotropy

Among the many metals in nature, certain metals show ferromagnetic ordering at room temperature. These materials are typically iron, cobalt, and nikel in the 3d transition metals. The magnetism of such a magnetic material is manifested by an exchange interaction, which is a Coulomb interaction between an electronic charge in the material and the antisymmetric law of quantum mechanics [2,3]. When the sign of exchange interaction is positive, ferromagnetic ordering arise. In general, these ferromagnetic materials show energy dependence to the direction of magnetization, which is magnetic anisotropy.

In bulk ferromagnetic materials, magetic anisotropy prefers in-plane magnetic anisotropy (IMA), because of the demagnetizing field of material itself. However, as the technology for growing metal thin films has been developed, it has become possible to manufacture magnetic thin films with a thickness ranging from several ongstrom to several nm. In this ultrathin magnetic thin film, interface and surface is dominant over the bulk effect. As a result, the alignment of magnetization to the direction perpendicular to the film plane, which is perpendicular magnetic anisotropy (PMA) arise [4].

PMA in ultrathin film structure was studied at various Ferromagnet/Heavy metal multilayer structures, Pd/Co [5], Pt/Co [6], Au/Co [7], Ir/Co [8] and so on [9]. When an external magnetic field to the perpendicular direction of film plane is applied to a magnetic thin film having PMA, by 1) impurity that existed before deposition on the film substrat, 2) lattice mismatch that occurs during deposition, damage to the substrate after deposition, etc there exist variation of anisotropy to the magnetic film. From this nucleation sites which has lower anisotropy than the surround, magnetic domain wall can be nucleated probabilistically by thermal fluctuations [10].

Within this PMA system, magnetization intrinsically shows only two binary state which is up or down except for the magnetization inside the domain wall (DW), which will be explained after. The energy of effective magnetic anisotropy can be described as

$$\mathrm{K}_{\mathrm{U}}^{eff} = \left(K_V - \frac{1}{2}\mu_0 M_s^2\right) + \frac{K_s^{tot}}{t_{FM}} \ [\mathrm{J/m^3}]. \qquad (1)$$

Here $\mathrm{K}_{\mathrm{U}}^{eff}$ is effective uniaxial anisotropy, $\mathrm{K_V}$ is volume anisotropy, $\mathrm{M_s}$ is saturation magnetization [A/m], $\mathrm{K}_{\mathrm{s}}^{tot}$ is total surface anisotropy. $\frac{1}{2}\mu_0 M_s^2$ term is demagnetization of film. Figure 1.1 is plot of $\mathrm{K}_{\mathrm{U}}^{eff} t_{\mathrm{Co}}$ with respect to $\mathrm{t_{Co}}$. The slop of blue fitted line is $K_V^{eff}(= \mathrm{K_V} - \frac{1}{2}\mu_0 M_s^2)$, and the intercept of y-axis is $\mathrm{K}_{\mathrm{s}}^{tot}$. PMA arise when the sign of $\mathrm{K}_{\mathrm{U}}^{eff}$ is positive.

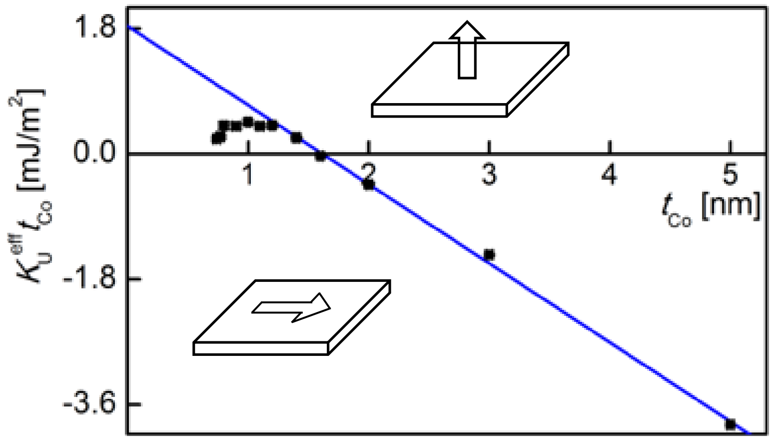

Figure 1. 1 Plot of $\mathbf{K_U^{\mathit{eff}}}\boldsymbol{t_{Co}}$ with respect to $\mathbf{t_{Co}}$ [11].

1.2 Magnetic Domain Wall

As already mentioned, when we applying external magnetic field parallel to z direction, magnetic domain can be nucleated.

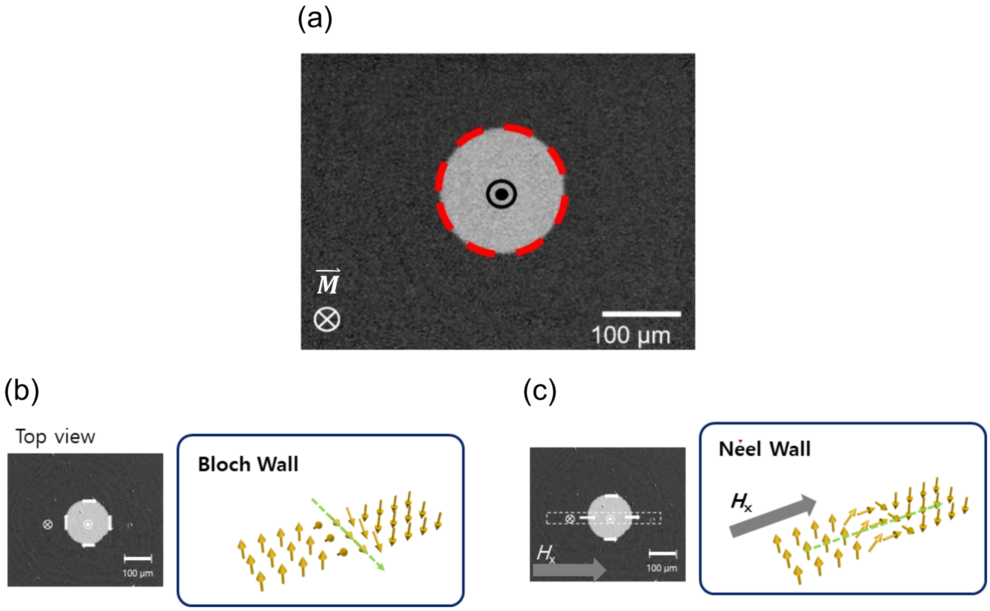

Figure 1. 2 Image of magnetic DW, which is illustrated as ref dashed line and acquired by use of full field polar magneo-optical Kerr effect microscopy. Dark region, which is out of DW, is magnetic domain with down direction and the bright region inside the DW is magnetic domain with up direction, (a). Bloch type DW, (b), and Neel type DW, (c). Magnetization inside the DW was represented as white arrow at left side of each figure. Gray arrow shows the direction of external in-plane magnetic field (H_x). More detailed spin configuration inside the DW was illustrated at the rught side of each figure. Yellow arrow shows direction of spin and the green arrow shows the averaged direction of magnetization inside the DW.

By use of microscopy with P-MOKE setup, image of magnetic domain was acquired as can be seen in Fig.1.2. Now here we focus on the more detailed spin configuration inside the DW. The magnetization inside the magnetic domain wall consists of discontinuous magnietzations with a specific width between two antiparallel direction of magnetic domain, which is up and down domains. This is due to the balance of exchange energy and anisotropy energy [2,3]. Magnetic domain walls can be classified according to the plane of rotation of magnetization in side the wall. When the magnetization rotates parallel to the plane of DW, it is called as Bloch type DW (Fig. 1.2. b). When the magnetization rotates in vertical direction to the plane of DW, it is called as Neel type DW. (Fig 1.2. c).

By the demagnetizing energy inside the magnetic domain wall itself, Bloch typw DW is prefered. That's the reason why in-plane direction of external magnetic field is applied in Fig 1.2. c. However in some special situation even without in-plane external magnetic field Neel type domain wall is favored, which will be explained later.

1.3 Measurement of Magnetic Domain Walls

Without any explanation we already mentioned polar magneo-optical Kerr effect (P-MOKE) microscopy here we describe the principle of P-MOKE. The measurement method of magnetic DW can be done in many different ways. On the one hand, it can be directly measured through the long-range dipolar interaction, which is the principle of MFM (Figure 1.3). On the other hand, DW can be measured indirectly via interaction between the measurement source and magnetization of magnetic thin film. Measurement source of indirect methods can be light or an electron. In this chapter we discuss about the principle of polar magneto-optical Kerr effect and anomalous Hall effect.

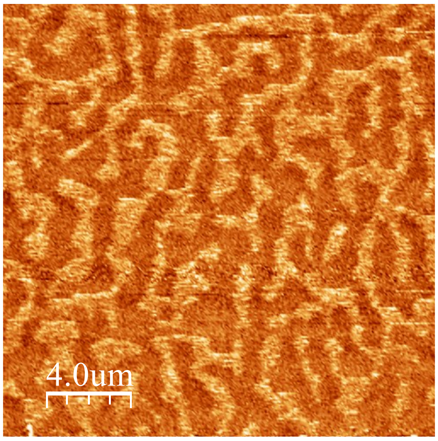

Figure 1. 3 MFM image of domain pattern with PMA at magnetic thin film. MFM (Nanofocus. Co) was measured 20 μm by 20 μm size. Two different brightness of image shows two different direction of magnetic domain. (Measured by S.-H. Lee)

1.3.1 Magneto-Optical Kerr effect

If one shed light on the surface of conductor, light will be reflected. Reflection of light can be thought as the radiation of electromagnetic wave by the acceleration of electron of conductor by the incident electromagnetic wave, which is light. If one repeats the same behavior to the magnetic material, there exist lorentz force due to the magnetization inside the magnetic maerial. Then, the direction of acceleration of electron inside the magnetic material will be different with the electron inside the conductor. Resultantly the direction of polarization of reflected electromagnetic wave would be changed, which is the magneto-optical Kerr effect.

More precise process of measurement via our P-MOKE microscopy setup is as below. From the Hg lamp (Source : Mercury arc lamp, Osram. co), un polarized light are generated. Through the linear polarizer, lights are polarized and incident to the surface of film through the half mirror and objective lens. Then, depending on the direction of magnetization of magnetic thin film, axis of polarization and the ellipticity of polarized light are changed (Figure 1.4).

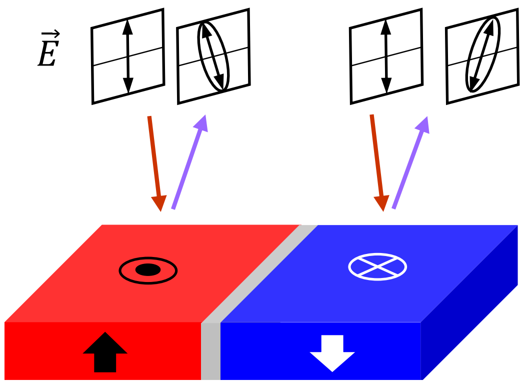

Figure 1. 4 Schematic illustration of polar magneto-optical Kerr effect. Axis of polarization is changed while the reflection of polarized light. Depending on the direction of magnetic domain, which is shown as red colored area with black circle and blue colored area with whied cross mark.

1.3.2 Anomalous Hall Effect

Since the first observation anomalous Hall effect, the mechanism of it was under debate for a long time. Because this effect was huge compared to the ordinary Hall effect, it was called as “anomalous”. In a present time, the mechanism of AHE is divided into intrinsic and extrinsic mechanisms [12-16].

Intrinsic mechanism describe AHE occur by the band structure. In a solid crystal, electrons are moved by the external electric potential. If we consider the electron in a solid crystal as bloch wave, moving electrons have spin dependent Berry phase, which results in aqusition of anomalous velocity. Anomalous velocity is vertical to the direction of current and spin, which makes electrons with antiparallel spins accumulate to the edge of material. Because this mechanism only depends on the bandstructure, this called as "intrinsic" [13].

Extrinsic mechanism describes that the AHE occur because of the impurity which has spin-orbit coupling. By the spin-orbit interaction between electrons and impurity, spin dependent scattering of electron occur. Finally, electrons accumulated to the edge of the material [14,15]. Resultantly, from these origins we can detect the z-direction of magnetization through the voltage difference between two transverse edge of magnetic wire or magnetic structure above the Hall bar structures (Figure 1.5).

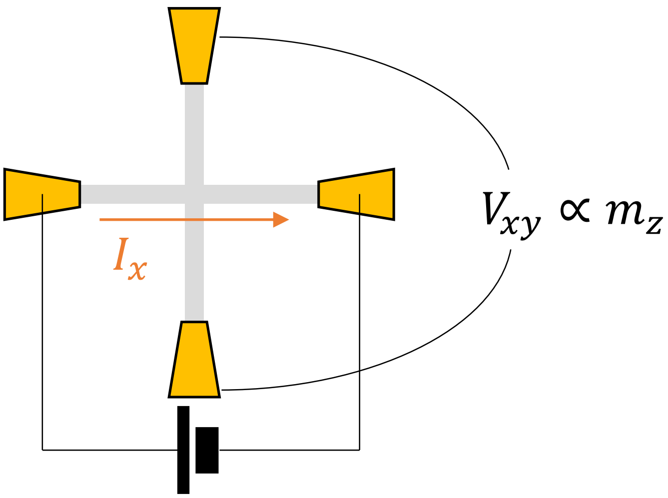

Figure 1. 5 Schematics of measuring anomalous Hall voltage. When the current is applied to the magnetic wire (I_x), by the anomalous Hall effect, voltage difference between the transverse edges of magnetic wire generated as V_{xy}

1.4 Dzyaloshinskii-Moriya interaction

From the pineeroring seminar work of phenomenological description of Dzyaloshinskii-Moriya interaction [17,18], quantitative calculations and experiments shows that DMI can occur in diverse magnetic system [17-21], including antisymmetric oxide [17,18], spin glass [19], and magnetic multilayer system [21] with the hamiltonian of $E_{\mathrm{DMI}} = -\vec{D} \cdot (\vec{S_i} \times \vec{S_j})$. As this antisymmetric exchange interaction manifest in these various systems, the microscopic origin of DMI also suggested in different pictures. Especially in metallic trilayer system, the mechanism of DMI is known to the scattering of electron between the adjacent atomic magnetic moments medated by impurity atoms. Calculation based on the Ruderman-Kittel-Kasuya-Yosida interaction with consideration of spin-orbit coupling of impurity atom was done by A. Fert and P. M. Levy [19]. Because DMI favor antisymmetric configuration of local magnetic moments, the PMA film with DMI shows chiral Neel type DW as shown in Fig. 1.6 [22,23]. Without DMI, magnetic moments favor parallel alignment each other by exchange interaction in ferromagnetic system, Fig. 1.6.a. However, with the existence of DMI, magnetic adjacent magnetic moments favor antiparallel alignment each other as seen in Fig. 1.6.b. When the energy of DMI is large enough, compared to the energy of demagnetization of magnetization inside the DW, DW can be stabilized as chiral Neel type, as seen in Fig 1.6.c. The point that we focus in this type of DW is the status of magnetization. As already shown in a Fig. 1.2.c, we can also make DW as Neel type without DMI. However, what is main difference between two DW is the direction of magnetization inside the DW. All of the magnetization inside the DW in

Fig 1.2.c[1], is parallel to the direction of external in-plane magnetic field, however the magnetization inside the DW in Fig 1.6.c shows all different direction of magnetization, which is showed as white arrow to the full-field MOKE image of magnetic domain. As one can see from the figure 1.6.c, magnetization inside the DW is directed to the outward from the center of DW. That's why we call it "chiral" Neel wall.

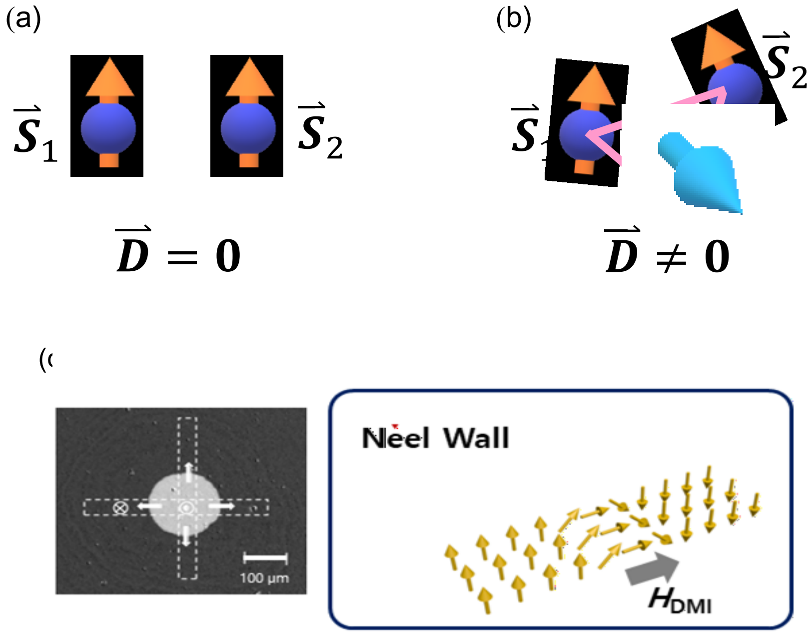

Figure 1. 6. Schematic illustration of Dzyaloshinslii-Moriya interaction. The blue sphere represents magnetic atom with spins, which is orange arrow. Without DMI, a, spin configuration favor parallel each other. With DMI, b, spin configuration prefers

[1] Here we would call this type of DW as "artifial" Neel type DW. Because without the external in-plane magnetic field, the magnetization inside the DW would re align with the plane of DW, which is Bloch type DW. This is similar situation when we apply in-plane magnetic field to the PMA magnetic film. If the applied magnetic field is large enough to realign the magnetization of PMA film to the in-plane direction, it would instantly align with the direction of magnetic field. However, just after we turn off the magnetic field, the magnetization simultaneously aligns with the easy axis, which is perpendicular to the film plane.

antisymmetric configuration each other. Gray sphere is adjacent impurity atom, Sky-blue colored arrow is Dzyaloshinskii-Moriya vector, and pink triangle means the interaction between the impurity and local magnetic moments. Left image shows full-field MOKE image of magnetic DW, where white arrow shows the direction of magnetization inside the DW. More detailed spin configuration of chiral Neel DW is illustrated at the right side. Yellow arrow shows the direction of magnetization. The gray arrow shows the direction of effective magnetic field generated by DMI, which is directed to outward from the center of DW.

1.5 Spin-Orbit Torque

The fact that the magnetic domain wall can be moved by electric charge current inspired the question “what is the physics behind it and is there any possibility for the next-generation memory application? ”. The first explanation for the driving mechanism of current-induced domain wall motion was provided by Sloncweski as spin-transfer torque (STT). When the spin polarized conduction electron passing by the local magnetic moment, exchange of spin angular momentum between local magnetic moment and spin polarized electron occur. However, as follow-up experimental results show, it was reported that the direction of CIDWM is inverse to the direction of electron. It takes time to sattle down the debate about the origin of CIDWM and clarify the mechanism. As a new mechanism of current driven DW motion, here we discuss about spin-orbit torque (SOT).

SOT is much more efficient than the conventional STT, and the direction of

CIDWM depended on the structure of magnetic fhin films② [24,25]. The main theories that explain the mechanism of SOT are spin-Hall effect [26-31] and Rashba effect [32,33]. The first mechanism, spin-Hall effect, share the same microscopic origin with anomalous Hall effect. When the charge current is applied, electrons with spin interact with the atoms of conducting material through the spin-orbit coupling. As a result, depending on the direction of spin of electron, scattering trajectories are different and finally, electrons with antiparallel direction of spin are accumulated to the edge of conducting material. If the conducting material is ferromagnetic material, there is difference in the density of states of electron with respect to the direction of spin. Due to the different number of accumulated charge, voltage difference between the two edge of ferromagnetic wire generated. This is anomalous Hall effect. However, if the conducting material is non-ferromagnetic material, there is no voltage difference but only accumulation of antiparallel directions of spins at each edge of conducting material③ (Figure 1.7).

② Sometimes this fact confuses the experimentalists. Because only with the direction of CIDWM, here we cannot distinguish whether the main driving spin-torque is originated from STT or SOT (When the direction of CIDWM is antiparallel with current) [33].

③ Because there is no voltage difference, it is hard to detect the spin Hall effect by electrical method. However, J. E. Hirsch proposed by measuring Hall voltage which is generated by spin current, one can detect the spin Hall effect [35].

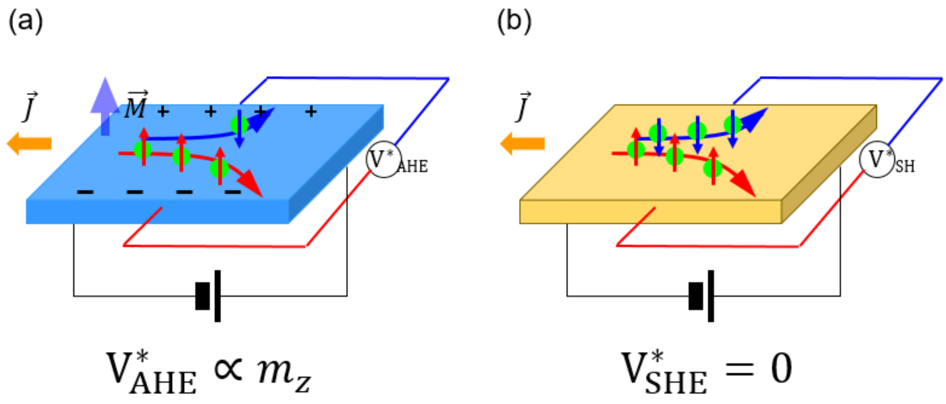

Figure 1. 7 Comparison between anomalous Hall effect(AHE) and spin Hall effect(SHE). Sky-blue colored cubiod is ferromagntic material(a) and yellow colored cubiod is non-ferromagnetic material, where blue colored arrow is the direction of magneitzation, green sphere is the electron, blue(red) arrow on the electron is down(up) direction of spin

The second mechanism, Rashba effect, occur at the interface between ferromagnetic material and adjacent layer. Because of different material structure in z-direction, there occur effective electric field. When the electron accelerated in the electric field, they feels effective magnetic field due to the relativistic effect. As a result their spins are polarized and accumulated at the interface. In general, spin torque by SOT exert torque on the DW with direction of $\hat{m} \times (\hat{m} \times \boldsymbol{\sigma})$ and strength of $J\varepsilon_{sat,SOT}$.

$$\tau_{SOT} = J\varepsilon_{sat,SOT}\hat{m} \times (\hat{m} \times \boldsymbol{\sigma})$$

where J charge current density, $\varepsilon_{sat,SOT}$ maximum intensity of SOT efficiency, $\hat{m}$ directional vector of magnetization inside the DW, and $\boldsymbol{\sigma}$ directional vector of spin generated by SOT.

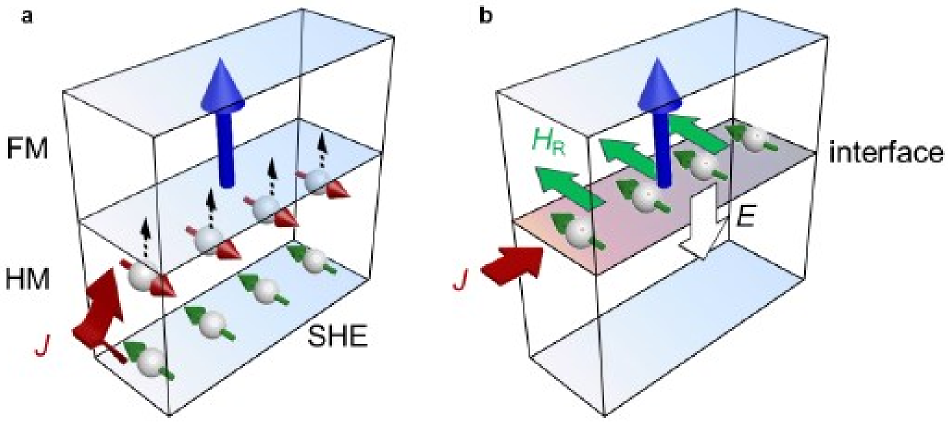

Figure 1. 8 Schematic illustration of spin-orbit torque arising from a, Spin-Hall effect and b, Rashba effect. The red arrow shows the flow of charge current, white sphere shows conduction electron, red and green arrows piercing white sphere is electron's spin. The blue arrow indicates the direction of effective magnetic field induced by SOT.

1.6 Quantifying method of SOT & DMI by spin torque efficiency measurement

In experimental situation, two mechanisms includin SOT and DMI are described as effective magnetic field. Based on the analysis of DW depinning field which is the field that the DW starts to move, we can measure the effective field of SOT and DMI step by step [24,36-38].

1.6.1 Measurement scheme of spin-torque efficiency

While measuring the depinning field of DW, we can apply charge current which is low enough not to move DW without magnetic field. Then, as mentioned in previous chapter, spin torque generated by SOT exert torque which is proportional to $J\varepsilon_{\mathrm{sat,SOT}}$. As shown in figure 1.6 (a), firstly DW is initialized inside the micro patterned wire. Nextly, we can measure the depinning field with charge current applied on magnetic wire as shown in FIG. 1.6 (b). By measuring depinning field with different current density, we can observe, as shown in FIG 1.6 (c), the linear proportionality of depinning field with respect to the current density with the relation $\mathrm{H}_{\mathrm{SOT,z}} = \varepsilon J$ where ε is spin-torque efficiency.

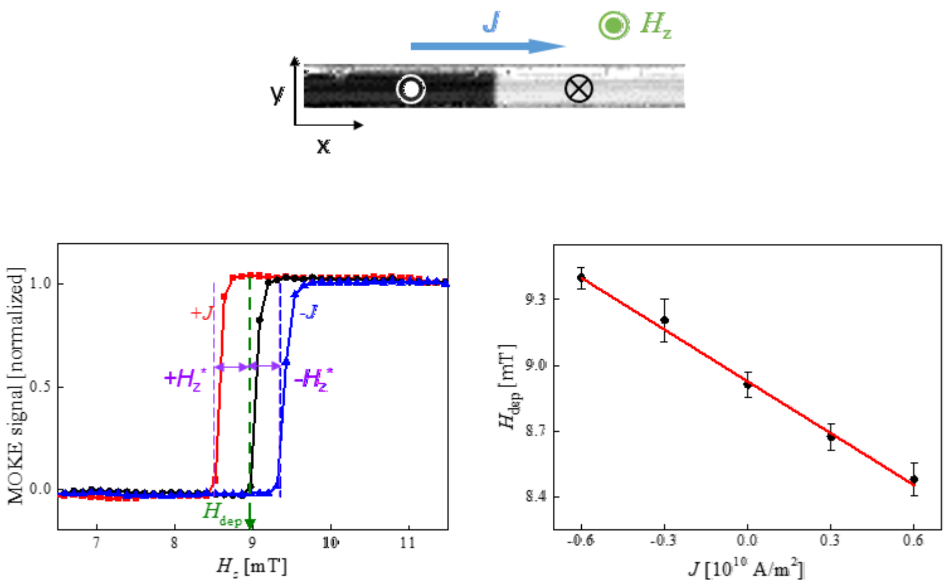

Figure 1. 9 Measurement scheme of depinning field (H_{dep}) with external magnetic field (H_z with green circle) and charge current (J with sky-blue colored arrow). On the image of magnetic wire, direction of magnetic domain is shown as white circle and cross mark, (a). By use of scanning P-MOKE instrument, MOKE signal with respect to the z-direction external magnetic field was measured. Depinning field, H_{dep}, is the field that DW starts to move. As a result, depinning field was defined as the field where the MOKE signal is uprising. To measure the spin-torque efficiency, depinning field with the positive and negaive bias of current density was measured, (b). Linear proportionality of depinning field with respect to the charge current density. The ratio between the variation of depinning field over current density is spin-torque efficiency, which is the slope of the graph (ε), (c).

1.6.2 Analysis of spin-torque efficiency with respect to in-plane magnetic field

Magnetization configuration inside the DW is manifested by the competition between the diverse energies. Energy of magnetic DW can be characterized as

$$\sigma = \sigma_0 + 2K_D\lambda\cos^2\psi - \pi\lambda M_S(H_{DMI} + H_x)cos\psi$$

where σ DW energy, σ_0 Bloch wall energy, K_D DW anisotropy energy density, λ width of DW, ψ polar angle of magneitzation, H_{DMI} effective in-plane field of DMI, M_s saturation magnetization, and H_x external in-plane magnetic field [22,24,32,39,40]. With DMI and external in-plane magnetic field, equilibrium state of magnetic DW can be determined as

$$\text{Neel type DW } (\psi = 0 \text{ or } \pi): \; H_{DMI} + H_x > 4K_D/\pi M_S, \; \cos\psi = 1 \text{ or} -1$$

$$\text{Intermediate } (\psi \neq 0, \pi, \text{and } \pi/2): \; H_{DMI} + H_x < 4K_D/\pi M_S \;, H_x \neq -H_{DMI}$$

$$, \; \cos\psi = \pi M_S(H_{DMI} + H_x)/4K_D$$

$$\text{Bloch type DW } (\psi = \pi/2): \; H_x = -H_{DMI}, \; \cos\psi = 0$$

In experimental situation DMI can be understood as effective in-plane magnetic field, H_{DMI}, acting on the magnetization inside the DW. As shortly mentioned in chapter 1.2, Bloch type DW is preferred because of magnetostatic energy. However, with the existence of DMI, DW can be stably maintained with Neel type.

Effective magnetic field ($H_{\mathrm{SOT,z}}$) generated by SOT is $J\varepsilon_{\mathrm{sat,SOT}}m_x$, where m_{x} is x component of unit magnetization inside the DW. As shown above, m_{x} is changed from -1 to 1 by applying H_{x}.

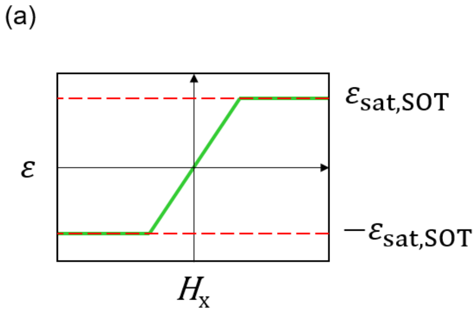

Figure 1. 10 Schematic illustration of spin-torque efficiency (ε) with respect to H_{x} without $\mathrm{H_{DMI}}$, (a), and with $\mathrm{H_{DMI}}$, (b). Green line shows the spin torque efficiency, red dashed line shows saturation spin-torque efficiency by SOT, and sky-blue colored line shows the offset from the axis at $H_{\mathrm{x}} = 0$, which is the reversed sign of value of effective DMI-induced in-plane magnetic field.

Figure 1.10 shows the schematic illustration of spin-torque efficiency with respect to H_{x}. By applying in-plane magnetic field, we can efficiently move DW with charge current. However, with the existence of DMI, DW can be efficiently moved by charge current without any in-plane magnetic field [37,41,42].

Chapter 2 Sample Fabrication

One of the remarkable technological advances in 21th century is fabricating method. Among the different kinds of method, physical vapor deposition was widely used. In th ultraclean envireonment, pure metal atoms can be deposited by some sources of deposition. Also improvement of performance enable one to reach the ultrathin film structure, which is different with bulk structure. In this chapter we will discuss about the description of fabrication system and process, experimental system development, analysis on the magnetic property of magnetic thin films, and device fabrication.

2.1 Description for sputtering system & process

PMA is a phenomenon that occurs due to the interfacial effect between the magnetic material and the adjacent metal layer when the thickness of the magnetic material reaches several angstroms. Here we use commercially diced 4-inch diameter Si 525 um/ SiO_2 100 nm substrate (prime grade, 1-10-ohm cm, p-type, crystalline orientation <100>, dry oxidation by furnace).

By using cavitation generated by ultrasonic in acetone and methanol, we can clean the surface of substrate. Then we load the chuck to the load-lock chamber with base pressure ~ 10^{-7} torr.

Before we describe the sputtering precess, shortly, sputtering is to transfer the momentum obtained by accelerating the ionized gas particles by attaching a cathode to the metal target to be deposited in an inert gas (Ar, Kr, Xe,) environment where there is little chemical reaction. Thus, as the ionized gas particles collide with the surface of the metal, the metal atom is separated from the target surface and deposition begins.

(a)

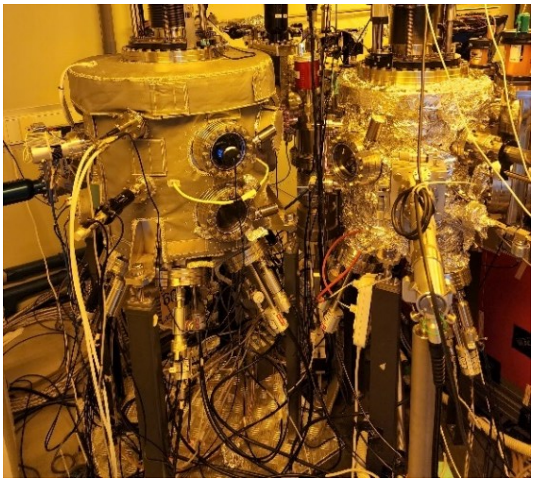

(b)

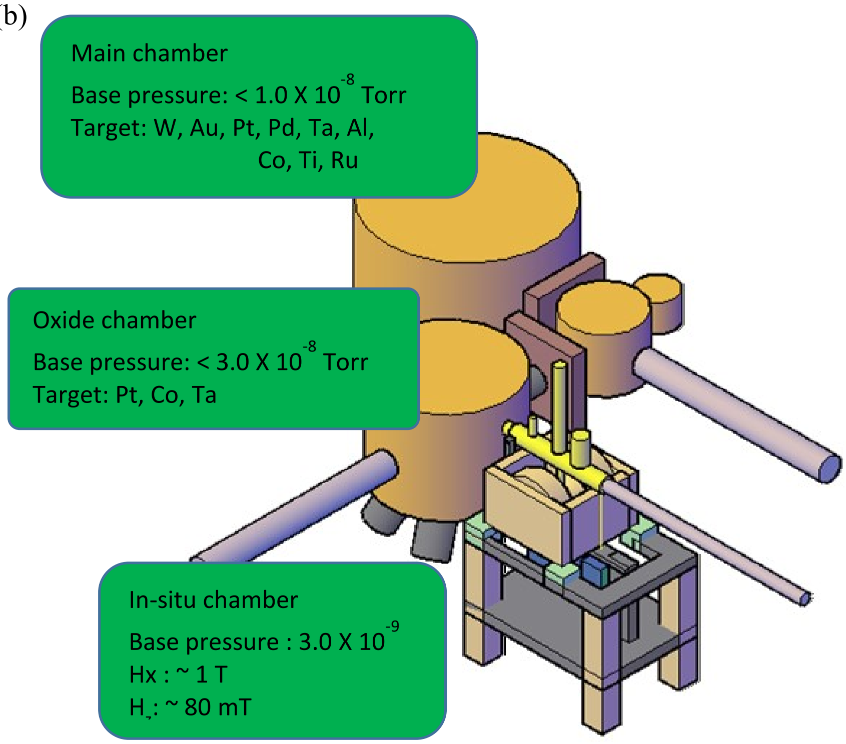

Figure 2. 1 DC

vacuum chamber system, b.

As shown in figure 2, our DC magnetron sputtering chamber is maintained in ultra high vacuum (UHV) order of 10^{-8} torr by cryo pump and it consists of 7 sputtering guns, which enable us to sputtering diverse metals. Load-lock chamber and oxide chamber also maintained in UHV by turbo molecular pump.

After enough vacuum environment was acquired in load-lock chamber, we should make main chamber to sputtering environment. The first thing to do is purging the Ar gas about 10 minutes. Because while we don't use sputtering, the Ar gas pipe (1/4 inch, stainless) contaminated by external impurity. Also pre-sputtering of target material should be done, because of the same reason at the purging.

After transferring the substrates from load-lock chamber to main chamber, stage is lowered down to have low distance (15 cm) between substrate to target (2 inch, R&D korea). By applying cathod voltage to the target and opening the shutter, deposition started. During this deposition process, plasma should be maintained at a stable power.

2.2 Experimental system development

As PMA arise at the ultrathin ferromagnetic layer thickness, sputtering system should be able to control the thickness in reproducible way. For the precise control of sputtering thickness, deposition rate was low enough. However, the control method of shutter was implemented in human controlled swtich. Because this way can involve human error during the sputtering or unreliable thickness of material, here we develop the way of controlling shutter switch to computer-based system.

Firstly, Arduino (UNO board) was connected with computer via RS-232 comunication. In addition, relay switch was also connected to the adress of arduino. Finally, shutter time of sputtering was controlled by computer by using Labview. With this system to monitor the status of deposition in real-time, we additionally set up the quartz crystal monitor (QCM). This QCM also communicate with computer during the sputtering. As seen in figure 2.2, sputtering system was set up.

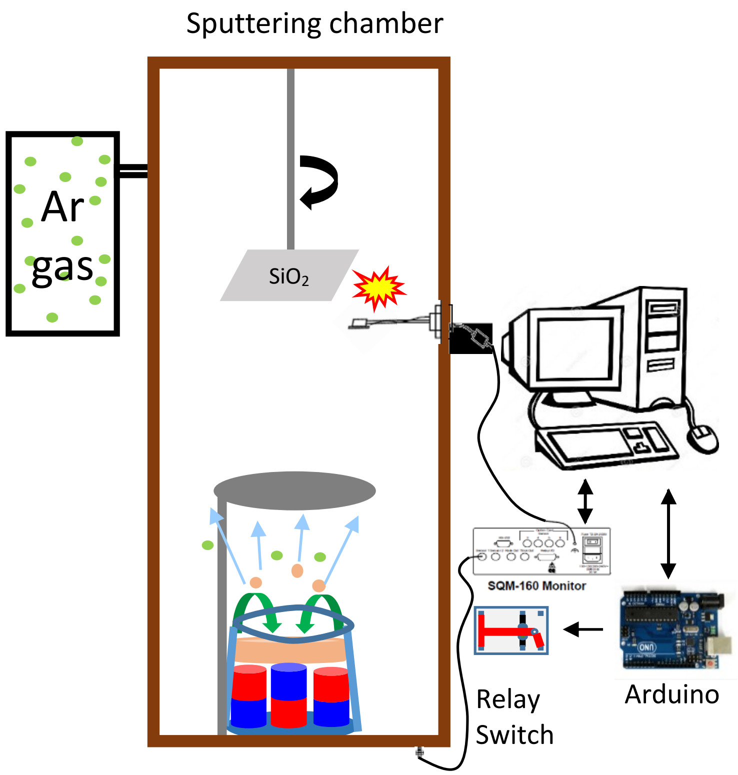

Figure 2. 2 Schematic illustration of sputtering system. With the process gas (Ar, Green sphere), from the sputtering gun which is position at the bottom of figure. Sputtering gun is composed of permanent magnet (SmCo, north pole with red cylinder and south pole with blue cylinder), sputtering target (ivory colored cylinder), and gun shutter (grapy cylinder and ellipse). Magnetic field by permanent magnetic was illustrated as green colored arrow. Top of the figure, Si substrate is rotated while sputtering process occur. Right side of the chamber, quartz crystal is positined. Quartz crystal communicate with thickness monitor

controller through BNC cable and the controller communicate with PC through RS-232 to usb cable. By use of Labview, here we control the mechanical movement of sputtering shutter by transferring the 5 V voltage control from the Arduino to relay switch, which controls the solenoid valve of air pressure pipe.

2.3 Reproducibility check by analyzing DW velocity

Just as important as preparing PMA samples with different compositions and new structures is to compare the properties of the samples produced present with thoes of samples of the same composition in the past. This property can be found by analyzing the speed of the DW with respect to the external magnetic field [43,44].

2.3.1 DW motion by external magnetic field

In addition, these magnetic DWs interact with pinning sites caused by local defects that are randomly located throughout the magnetic film. These pinning sites cannot be traveled below a certain external field, but if there are thermal fluctuations, the magnetic DW can probably pass even below the depinning field. This motion of magnetic DW called as “creep” as shown in figure 2.3 [45-48].

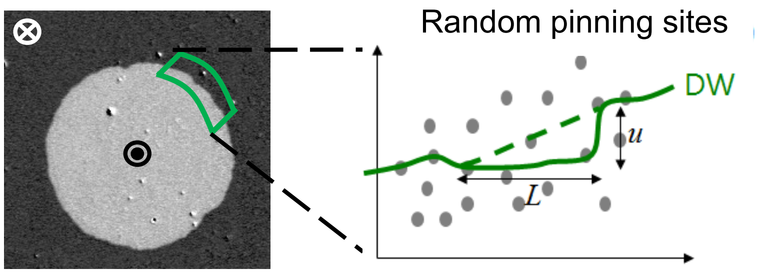

Figure 2. 3 DW in a disordered pinning sites. Magnetic domain image acquired by full-field MOKE microscopy (the image was acquired by subtracting the image which is down saturation state to the image where there is magnetic domain wall). The dark region shows down direction of magnetization and bright region shows up direction of magnetization (left). Schematic illustration of pinning site when we magnify the area inside the green lines. Pinning sites (gray circle) are randomly distributed with respect to the film plane (right). With the competition between elastic energy and pinning energy, DW (green line) has its roughness (not a straight line as green dashed line).

We can comprehend the creep motion by considering the free energy experienced by DW in a pinning potential. Free energy experienced by DW is

$$F(u,L) = \varepsilon_{el}\frac{u^2}{L} - (\Delta\xi^2 L)^{\frac{1}{2}} - M_s HtLu$$

Where ε_{el} is the elastic energy per unit length, u is the amplitude of DW, L is the length of DW, Δ $(= \mathrm{f}_{\mathrm{pin}}^2 \mathrm{n_i} \xi)$ scales the pinning strength of the disorder, ξ is the charastic length of the disorder potential, M_s is saturation magnetization, H is external magnetic field, f_{pin} is local pinning force, n_i is the surface density of pinning centers, and t is thickness of ferromagnetic layer.

After some calculation, which is well described in Ref. 45, velocity of DW can be described as

$$v_{DW} = v_0 \exp(-\alpha H^{-\frac{1}{4}})$$

Now if we follow the calculation process in Ref. 44, here we can derive the relation between the creep constant and thickness of ferromagnetic layer as $\alpha \propto t$.

Therefore, in the next section, we will discuss whether the thickness of the ferromagnetic layer is well controlled through the analysis of magnetic DW velocity with respect to the external magnetic field.

2.3.2 Reproducibility check

As reproducibility starts from comparing the magnetic property within the same structure but made in a different time of fabrication, here we need for the data from the past reports. The sample structure, which is well-known for manifesting PMA and employed for DW experiment from the early days of research on PMA to nowadays [6,9,10,11,22-25,31,38,44,45,47,49], is Pt/Co/Pt. Thus here we choose to use Pt/Co/Pt magnetic ultrathin film structure as a tools to check the status of our DC magnetron sputtering chamber, which is reproducibility.

Among the lots of magnetic parameters (total magnetic moment, magnetic anisotropy field, coercive field and so on) here we decide to use the creep constant as a factor of reproducibility④. Thanks to the pioneering work done by D.-Y. Kim et al [44], dependence of creep scaling constant with respect to the ferromagnetic layer shows not only clear monotonic increase but distincting between different thickness of ferromagnetic films.

By use of our full-field MOKE microscopy, creep behavior of magnetic domain wall in Pt/Co/Pt was analized. After saturating magnetization to down direction, z-direction of magnetic pulse, which is large enough to observe the reversed magnetic domain but not to fully saturate the magnetic film as up direction, was applied. Then with respect to the intensity of magnetic field, image of magnetic domain wall was captured by CCD camera. By subtracting the background image from the captured image, position of magnetic domain wall was defined and calculated to the velocity of magnetic domain wall. This process of analysis was done for every Pt/Co (t_{Co})/Pt films with t_{Co} range from 0.3 nm to 0.6 nm with 0.05 nm increment. After plotting the speed of DW with respect to the z-direction magnetic field in log scale, here we can observe the clear linearlity with the creep scaling constant (α), as shown in figure 2.4.a.

---

④ Other magnetic parameters can be confused to check the reproducibility. For example, anisotropy field is not a monotonic increase value with respect to the thickenss of ferromagnetic layer, as can be seen in Fig. 1.1, coercive field is affected by the extrinsic factor such as nucleation site. However, measuring magnetic moment can be used for confirming reproducibility though we don't have tool to measure it. But here we use ultrathin thickness of ferromagnetic layer, which is a few monolayer, sensitivity to measure the total magnetic moment of each film should be good enough.

By use of forementioned creep equation, we can measure the velocity of DW with respect to the external magnetic field as in figure 2.4. a. As a comparison data, here we refer the data from ref. 44 (Fig.2.4. b). One can see from the Figure 2.4. b and c that the reproducible state of our sputtering system was well maintained at 2019. As a whole, one can see clear consisency between different data sets (Fig.2.4.e).

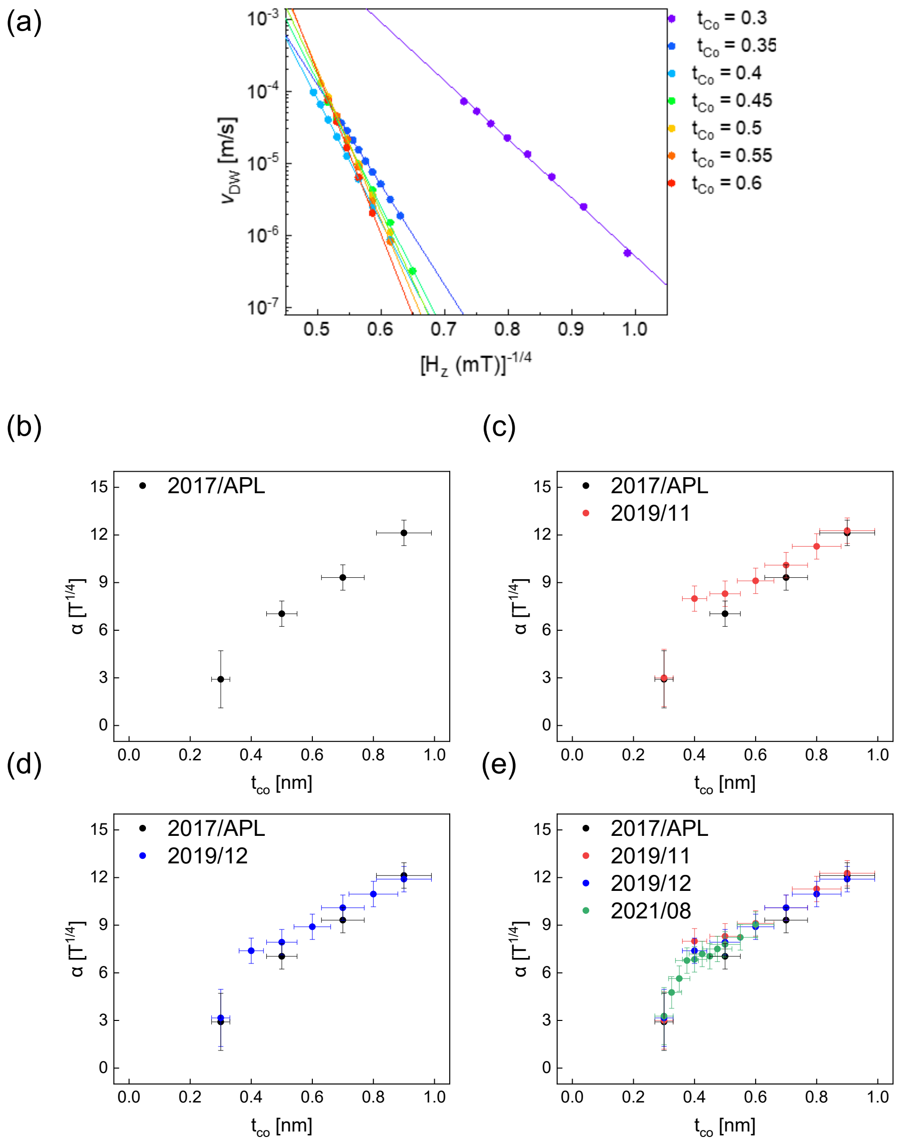

Figure 2. 4 DW velocity with respect to the external field in Pt / Co (t_{co}) / Pt trilayer. Speed of DW with respect to the z-direction external magnetic field was measured using full-field MOKE microscopy for the diverse variation of ferromagnetic layer thickness from 0.3 nm to 0.6 nm with 0.05 nm increments. Then the velocity of magnetic domain wall was plotted in log scale to calculate the creep scaling constant (α), a. Data of creep scaling constant from ref. 43 for the comparison data (b). Reproducibility check data at November, 2019 (c). Reproducility check at December, 2019 (d). Reproducibility check at August, 2021 and comparing all the data, (e).

2.4 Micro sized device fabrication

For the experiment which inject the current, we should make the magnetic thin film as a form of confined geometry. In general, to fabricated micro-sized device we use photo-lithography, ion milling, and lift off process as shown in figure 2.5 (a). In this section we describe the optimized condition for fabricating micro-sized device for electric measurement.

● Photo-lithography

Photolithography use light as source for transferring pattern to the surface of substrate or film. It consists of three steps, spin coating the photo-resist (AZ5214E, 4000 rpm, 60 s) and baking (90 degree, 90 ~ 95 s), exposuring (250 ~ 300 dose) ultra-violet light to the film, and developing (AZ MIF 300 or 500, 13 ~ 18 s with stirring) the exposured photo-resist. 4000 rpm, 60 s was decided by referring to the data shit from *microchem*. Baking degree was also choosed by referring to the same data shit. (In case of our magnetic thin film, too high temperature of baking can cause the degeneration of film quality).

● Ion milling

Our ion milling system consists of rotating sample stage with tilting angle from 0 to 90 degree. With the incident angle of 10 degree, Ar ion accelerated by accerator grid sputter the substrate. Then, to get rid of re-sputtered particle at the edge of patterned structure here we implement edge milling with incident angle of 15 degree. (our ion milling system use Kaufman-type ion source and power supply)

● Lift-off process

Lift-off process is litterly lifting off the materials above the PR. Generally, this process adopted to make the electrode or align mark. With proper time and power of sonication, deposited meterals can be easily detached from the substrate. However, in case of bad adhesion between substrate and electrode, lift-off process can severely degrade the quality of electrode (generally, adhesion of sputtered atom shows better quality than evaporated atom). If power of sonication is too strong, or time of sonication is too long, electrode can be damaged.

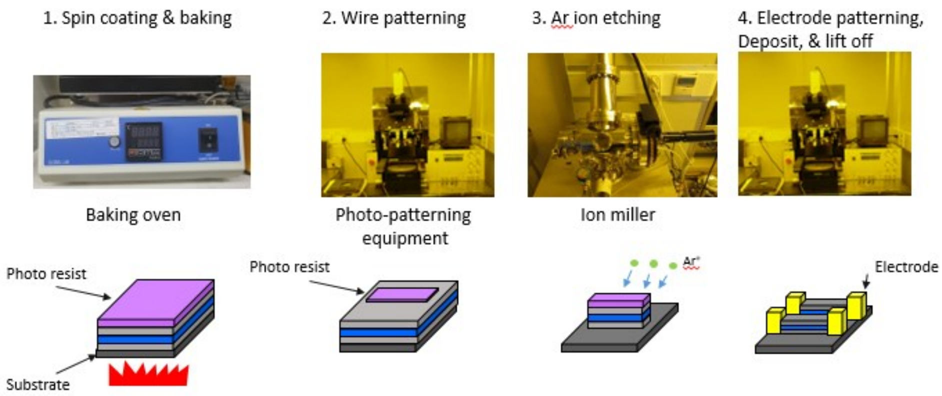

Figure 2. 5 Schematic illustration of device fabrication process

Chapter 3. Electrical Detection of DWs

Magnetic domain wall can be detected by using AHE which was mentioned in the background. It is important to electrically move and control the magnetic DW, but it is also important to read the position of the magnetic DW electrically. In many cases, magnetic tunnel junction is used to read the magnetization state, but MTJ structure is complicated and it is difficult to manufacture. In contrast, the measurement of the magnetization state using AHE is useful in measuring electrical transport despite its structural simplicity. In addition, it is possible to measure not only the magnetization state but also the DW motion. In this chapter a multifaceted analysis of electrical detection of DW has been described.

Chapter 3.1 Introduction

DW and its dynamics was widely studied for the physical phenomena and possibility for application [50-55]. In particular, magnetic domains can be used as digitalized data bits, and when the magnetic DW is electrically moved, its applicability also expands, so it is important to understand their characteristics.

In this chapter, here we report the empirical relation between the Hall voltage and DW position. Firstly, we measure and analyze the Hall voltage in each DW positions within many sets of combination between Hall bar width and wire width. Secondly, to find any relation between Hall voltage and DW position, here we implement numerical study by changing geometrical variables. Thirdly, we modify the Hall voltage equation to adopt in our experimental situation. Finally we checked that our approaches shows *converge* into single curve with empirical relation.

Chapter 3.2 Experimental approach

As many discoveries of new phenomena, the starting point of this study is a closer look at macroscopic phenomena. Using AHE, it is possible to know the magnetization state inside the Hall bar structure, and DW motion on the wire with the Hall bar as shown in Fig. 3. 1a can be compared with the conventional optical measurement and electrical measurement. Then, it can be seen that the difference in the measurement results appears as shown in Fig. 3. 1. b, which was initialliy predicted because the Hall bar has a physical width. However, as a result of examining the same experiment in more detail while changing the position of the magnetic DW, it was observed that the signal of the magnetic DW was also measured outside the Hall bar as in Fig 3. 1. c. (By courtesy of Y.-S. Nam & M. Kim)

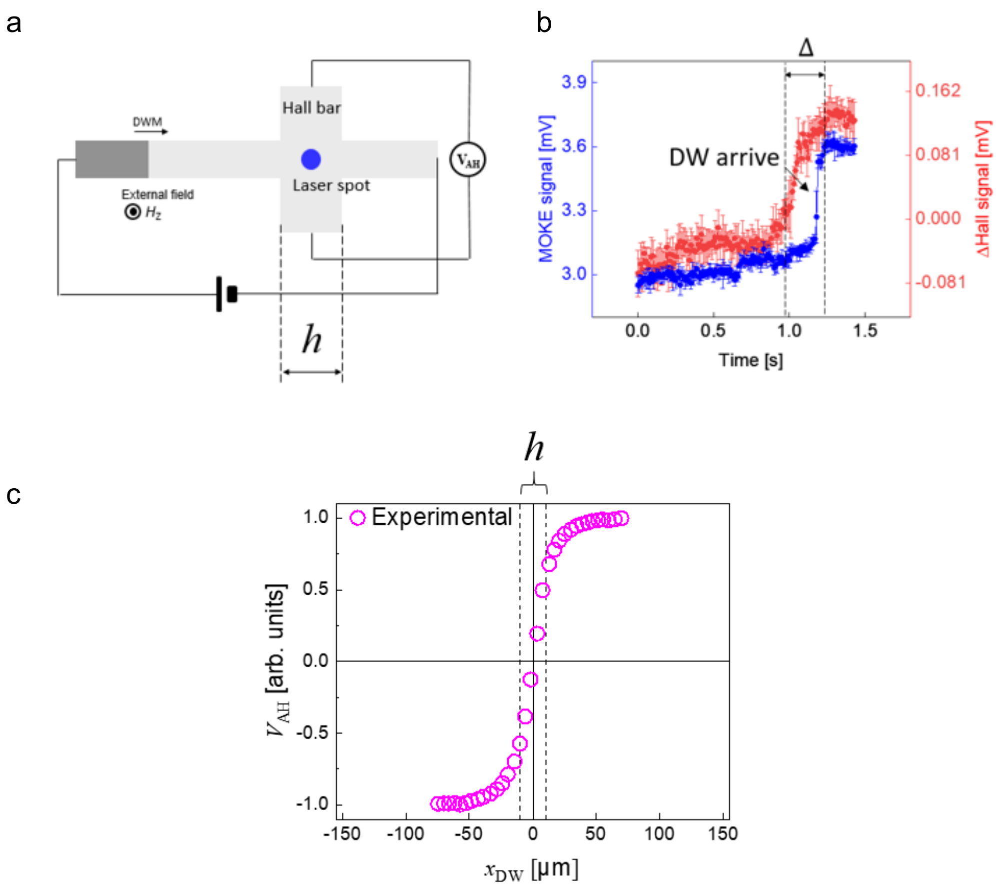

Figure 3. 1 Schematic illustration of experimental setup. The gray region of magnetic wire with Hall bar is magnetic domain with up direction. The other region is magnetic domain with down direction. Magnetic DW motion was detected by scanning P-MOKE. The blue circle means the detection area of scanning MOKE with the beam size is about 2 μm. Also, motion of magnetic DW was observed by measuring anomalous Hall voltage, a. Comparison between optical and electrical measurement of magnetic domain walll motion, b. Normalized anomalous Hall voltage by saturation status of magnetization was plotted

with respect to the position of magnetic DW which was confirmed by scanning the surface of wire. h is the width of Hall bar, c.

Chapter 3.2.1 Analyzing experimental results

First, in order to designate the range in which such a magnetic DW is measured, it was possible to fit various tangenthyperbolic functions on one graph as follows, and at this time, the detection rage could be defined as lambda. To denote the region where such a magnetic DW us measured, it was first possible to fit various tangenthyperbolic functions into a graph as follows, and at this point the detection range could be defined as lambda. That is, in the case of the first-order term of tangenhyperbolic function, the signal occupying about 76 % of the total signal is defined as the detection range. In order to investigate how this detection range appears in various Hall bar geometries, it was possible to fabricate various combinations of Hall bar width (h) and wire width (w), as shown in Fig. 3. 2. b through photolithography and ion milling process. As a result, figure 3. 2. c shows the 2-dimensional map of detection range with respect to the h and w.

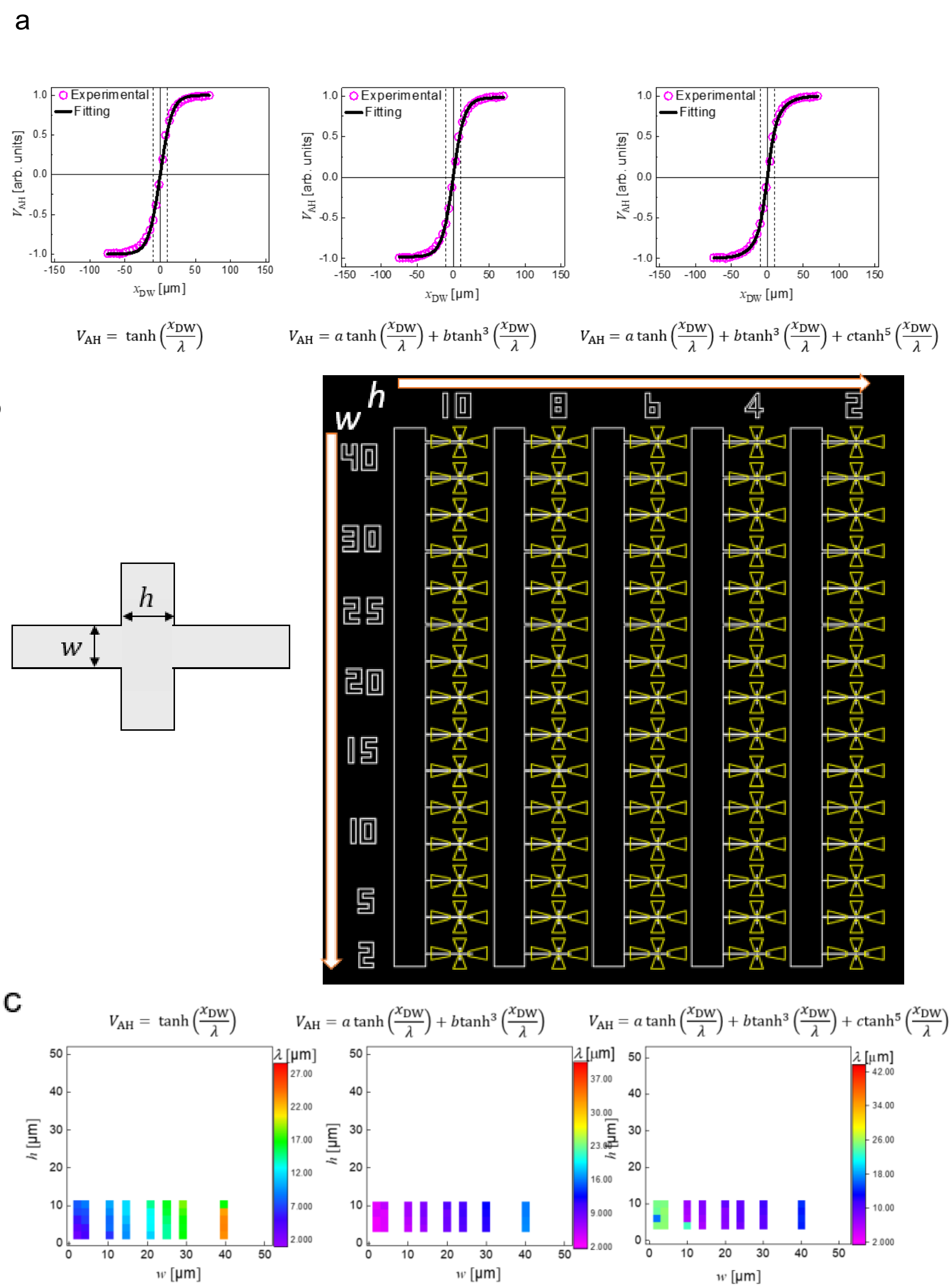

Figure 3. 2 The result of experiment was fiited with diverse combinations of odd power of tangenthyperbolic function, a. Schematic illustration of Hall bar structure, where wire width is h and Hall bar width is h (left) and CAD design of Hall bar structure (right), b. Detection range (λ) was plotted for various fitting functions in 2-dimensional map, c with respect to the w and h.

Chapter 3.3 Numerical Approach

To derive the empirical relation between geometric parameter and detection range, numerical simulation was conducted (Courtesy of M. Kim). By AHE, conductivity tensor in ferromagnetic wire can be described as

$$\boldsymbol{\sigma} = \begin{pmatrix} \sigma_0 & \mathrm{Sgn}(m_z) \times \sigma_{\mathrm{AH}} \\ -\mathrm{Sgn}(m_z) \times \sigma_{\mathrm{AH}} & \sigma_0 \end{pmatrix} \quad (1)$$

,where σ_0 conductivity and σ_{AH} anomalous Hall conductivity. In this geometry, σ_{AH} is proportional to the out-of-plane component m_z of the magnetization in the ferromagnetic films. Therefore, the maximum positive value of σ_{AH} is obtained when the magnetization is aligned along the $+z$ axis. Conversely, the maximum negative value of σ_{AH} is obtained when the magnetization is aligned along the $-z$ axis.

When an electric potential $\phi(x, y)$ is applied to the film, the current density $\mathbf{j}$ is generated through the relation $\mathbf{j} = -\ \boldsymbol{\sigma}\,\boldsymbol{\nabla}\phi$. It can be readily observed that $\mathbf{j}$ follows the continuity equation $\boldsymbol{\nabla} \cdot \mathbf{j} = -\sigma_0 \boldsymbol{\nabla}^2 \phi$ irrespective of the anomalous Hall effect. For the case of a steady state, the continuity equation can be written as $\boldsymbol{\nabla} \cdot \mathbf{j} = 0$ with the Laplace equation $\boldsymbol{\nabla}^2 \phi = 0$.

The boundary condition for the Hall bar geometry at the edge of the structure can be written as $\hat{\boldsymbol{n}} \cdot \mathbf{j} = 0$, where $\hat{\boldsymbol{n}}$ is the unit vector normal to the edge of the structure. It is considered that the Hall bar geometry has a wire width of w and Hall bar width of h within the simulation area of the horizontal length x_m and vertical height y_m as shown in Fig. 3.3a. A constant electric potential $\pm V_0/2$ is applied at the horizontal ends ($x = \pm x_m/2$) of the wire. The average electric potential difference between the vertical ends ($y = \pm y_m/2$) of the Hall bar is calculated as the Hall voltage.

The Hall bar structure is divided by unit square meshes of size Δ to construct the simulation geometry. The electric potential is written as $\phi_{(i,j)}^{(n)}$ with the lower indices (i,j) for the mesh at the position of $(x,y) = (i\Delta, j\Delta)$. The upper index (n) denotes the iteration number. Similarly, the current density can be written as $\mathbf{j}_{(i,j)}^{(n)}$. From the equation $\mathbf{j} = -\ \boldsymbol{\sigma}\,\nabla\phi$, $\mathbf{j}_{(i,j)}^{(n)}$ can be expressed as

$$\begin{aligned} j_{x}{}_{(i,j)}^{(n)} &= -\frac{\sigma_{\mathbf{0}}}{2\Delta}\left(\phi_{(i+1,j)}^{(n)} - \phi_{(i-1,j)}^{(n)}\right) - \frac{\sigma_{\mathrm{AH}}}{2\Delta}\left(\phi_{(i,j+1)}^{(n)} - \phi_{(i,j-1)}^{(n)}\right) \\ j_{y}{}_{(i,j)}^{(n)} &= -\frac{\sigma_{\mathbf{0}}}{2\Delta}\left(\phi_{(i,j+1)}^{(n)} - \phi_{(i,j-1)}^{(n)}\right) + \frac{\sigma_{\mathrm{AH}}}{2\Delta}\left(\phi_{(i+1,j)}^{(n)} - \phi_{(i-1,j)}^{(n)}\right) \end{aligned}, \quad (2)$$

where the first terms correspond to the diagonal contribution $\mathbf{j}_0$ from the longitudinal electric conductivity and the second terms correspond to the off-diagonal contribution $\mathbf{j}_{\mathrm{AH}}$ induced by the anomalous Hall effect. Finally, using the continuity equation $\nabla^2\phi = -\frac{1}{\sigma_0}\nabla\cdot\mathbf{j}$, an iterative equation can be developed to update $\phi_{(i,j)}^{(n+1)}$ expressed as

$$\begin{aligned} \phi_{(i,j)}^{(n+1)} &= \frac{1}{4}\left(\phi_{(i+1,j)}^{(n)} + \phi_{(i-1,j)}^{(n)} + \phi_{(i,j+1)}^{(n)} + \phi_{(i,j-1)}^{(n)}\right) \\ &+ \frac{\Delta}{8\sigma_{\mathbf{0}}}\left(j_{x}{}_{(i+1,j)}^{(n)} - j_{x}{}_{(i-1,j)}^{(n)} + j_{y}{}_{(i,j+1)}^{(n)} - j_{y}{}_{(i,j-1)}^{(n)}\right) \end{aligned}, \quad (3)$$

where the first term is obtained using the Laplacian $\nabla^2\phi$ and the second term is obtained using divergence $\nabla\cdot\mathbf{j}$. The boundary conditions are given as $j_{y}{}_{(i,j_b-1)}^{(n)} =$

0 at the nearest cell outside the bottom edge (i, j_b) and $j_{y\,(i,j_u+1)}^{(n)} = 0$ at the nearest cell outside the top edge (i, j_u) of the horizontal wire. Similarly, the boundary condition are $j_{x\,(i_l-1,j)}^{(n)} = 0$ at the nearest cell outside the left edge (i_l, j) and $j_{x\,(i_r+1,j)}^{(n)} = 0$ at the nearest cell outside the right edge (i_r, j) of the vertical Hall bar. The iteration is conducted until the system converges to a steady state with $\nabla \cdot \mathbf{j} = 0$, i.e., the maximum magnitude of $\nabla \cdot \mathbf{j}_{(i,j)}^{(n)}$ becomes less than a tolerance.

The present iterative algorithm was applied to the Hall bar geometry, where up (down) domain is placed left (right) to the DW as shown in Fig. 3. 3b. The simulation area was set to $x_m =$ 300 μm and $y_m =$ 100 μm with unit square meshes of 1 μm. The value of the tolerance δ was set to 10^{-2} A/m^3. The electrical properties were set as $\sigma_0 =$ 1.72×10^7 (Ωm)$^{-1}$ and $\sigma_{\mathrm{AH}} =$ 2.40×10^4 (Ωm)$^{-1}$ according to the values of Co [56,57]. The contribution from the DW was ignored, since the in-plane magnetization does not generate the anomalous Hall voltage and also, the DW volume is negligibly smaller than the Hall cross volume. The former is given by DW width × cross-sectional area and the latter is given by Hall bar length × cross-sectional area. Therefore, the ratio of the DW volume over the Hall cross volume is given by the ratio of the DW width (~a few nm) over the Hall bar length (~a few μm), which is typically in the order of 10^{-3}.

Figure 3. 3b depicts the simulation result of a case in which a DW is placed at the center of the Hall bar. The figure represents the two-dimensional planar distribution of $\mathbf{j}_{\mathrm{AH}}$. It can be observed that $\mathbf{j}_{\mathrm{AH}}$ had an antisymmetric distribution across the DW position. Therefore, the average value of $\mathbf{j}_{\mathrm{AH}}$ inside the Hall bar varied with respect to the motion of DW from the center of the Hall bar, resulting in the variation

of the Hall voltage. The blue symbols in Fig. 3.3c represent the simulation results of the normalized Hall voltage V_{AH} plotted with respect to the DW position x_{DW}, which rmatch well with the experimental result.

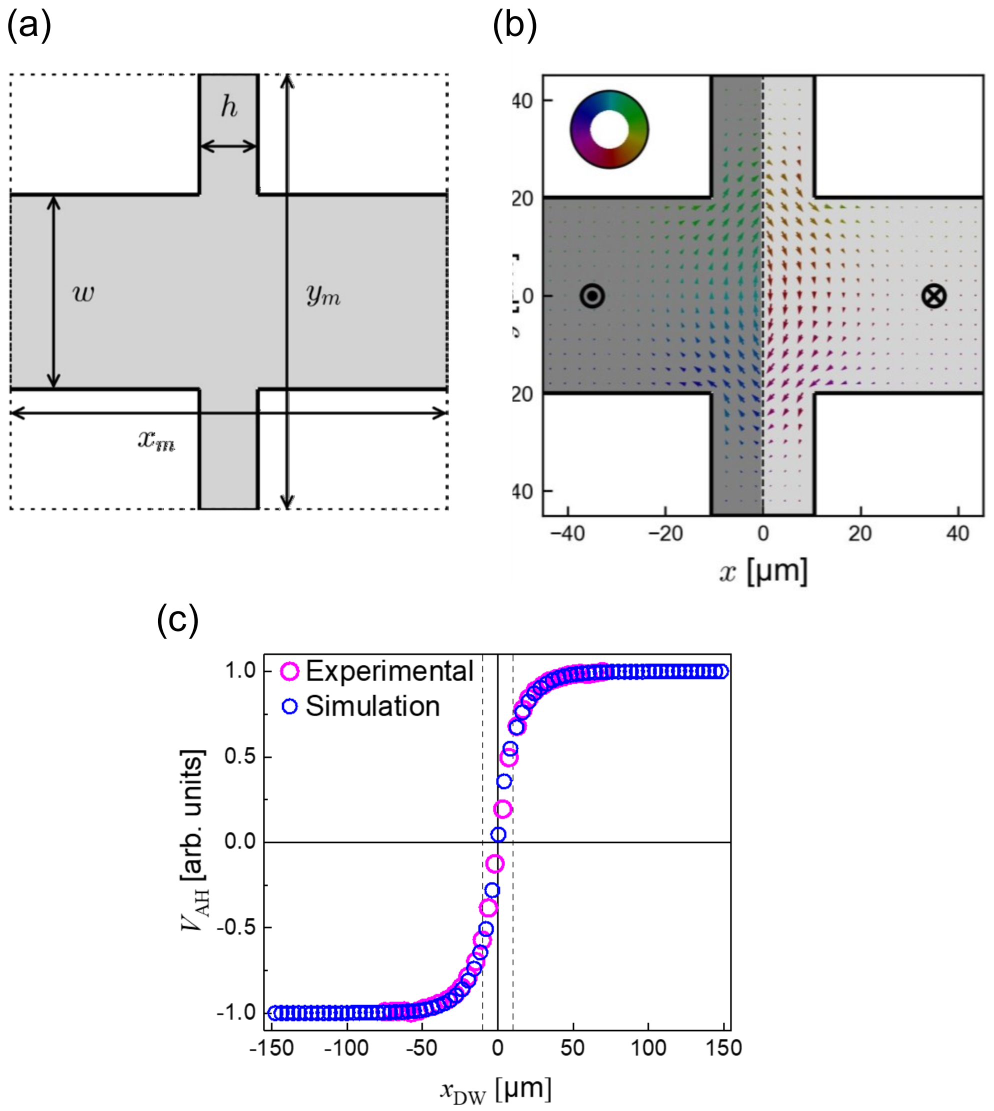

Figure 3. 3 a, Simulation geometry of the Hall bar structure with a wire width w and Hall bar width h in a simulation area with a width x_m and height y_m. **b**, Simulation result of the two-dimensional planar distribution of $\mathbf{j}_{\mathrm{AH}}$ when a DW is placed at the center of the Hall bar as shown by the vertical dashed line. The arrows indicate the vector $\mathbf{j}_{\mathrm{AH}}$, where the color corresponds to the direction according the circular color palette at the top-left

corner. The symbols ⊗ and ◉ indicate the direction magnetization. **c,** comparision of results between numerical simulation & experimental result.

Chapter 3.4 Analytical Approach

The simulation results were compared with that of the results an analytic equation to verify the validity of the simulation through simple geometrical consideration. Similar to that of the $\mathbf{j}_{\mathrm{AH}}$ distribution in Fig. 3.3b, Cheng *et al*. [58] investigated the distribution of the local Hall voltage v_{AH} in the vicinity of a DW. They demonstrated that v_{AH} is a function of the relative distance δx $(= x - x_{\mathrm{DW}})$ from the DW [58-60] which can be expressed as:

$$v_{\mathrm{AH}}(\delta x) \propto \mathrm{sgn}(\delta x)\left\{1 - \frac{8}{\pi^2}\sum_{n\ odd}\frac{1}{n^2}\exp\left(-\frac{\pi n|\delta x|}{w}\right)\right\}. \tag{4}$$

In the Hall bar geometry, the Hall voltage is determined by the average value over the Hall bar width. Therefore, in the case of a Hall bar with a width h in the range of $-h/2 \le x \le h/2$, the Hall voltage V^*_{AH} can be calculated as $V^*_{\mathrm{AH}}(x_{\mathrm{DW}}) = \frac{1}{h}\int_{-h/2}^{h/2} v_{\mathrm{AH}}(x_{\mathrm{DW}} - x)\, dx$. Combining Eq. (4) into the equation, V^*_{AH} can be expressed as:

$$V^*_{\mathrm{AH}}(x_{\mathrm{DW}}) \propto \begin{cases} \mathrm{sgn}(x_{\mathrm{DW}})\left\{1 - \dfrac{16w}{\pi^3 h}\displaystyle\sum_{n\,odd}\frac{1}{n^3}\exp\left(-\frac{\pi n|x_{\mathrm{DW}}|}{w}\right)\sinh\left(\frac{n\pi h}{2w}\right)\right\} & |x_{\mathrm{DW}}| > h/2 \\ \dfrac{2x_{\mathrm{DW}}}{h} - \dfrac{16w}{\pi^3 h}\displaystyle\sum_{n\,odd}\frac{1}{n^3}\exp\left(-\frac{n\pi h}{2w}\right)\sinh\left(\frac{n\pi x_{\mathrm{DW}}}{w}\right) & |x_{\mathrm{DW}}| \le h/2 \end{cases}. \tag{5}$$

The analytical formulae of Eq. (5) can be numerically evaluated. The green symbols in Fig. 3.4a represent the analytical results of $V_{\mathrm{AH}}^{*}(x_{\mathrm{DW}})$ for a Hall bar identical to that used in the simulation geometry. The perfect match between V_{AH} and V_{AH}^{*} verified the validity of the numerical simulation and analytic formulae.

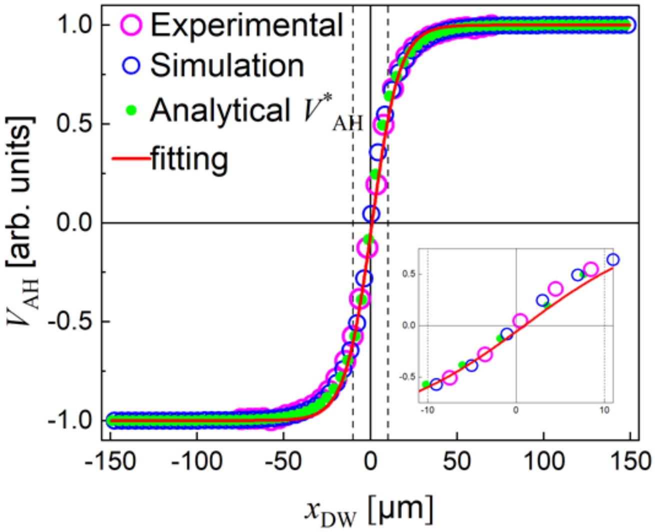

Figure. 3.4 Plot of the normalized Hall voltage V_{AH} plotted with respect to the DW position x_{DW}. The purple, blue, and green symbols represent the experimental, simulation, and analytical results, respectively. The red curve represents the best fitting with tanh function. Inset shows an enlarged view in the vicinity of $x_{\mathrm{DW}} = 0$.

Chapter 3.5 Result & Discussion

The two vertical dashed lines in Fig. 3.4a indicate the width of Hall bar. It can be observed that V_{AH} kept varying even when x_{DW} goes outside the Hall bar. This observation was in contrast to the general expectation that V_{AH} is sensible to magnetization solely inside the Hall cross. The broadening of the V_{AH} variation range was attributed to the non-local distribution of the current density in vicinity of the Hall bar geometry.

A series of simulations were performed by sweeping w and h to determine the relation between the broadening and Hall bar geometry. For each simulation result, the broadening was parameterized by the half width λ of the variation, by fitting the $V_{\mathrm{AH}}(x_{\mathrm{DW}})$ variation by $\tanh(x_{\mathrm{DW}}/\lambda)$. The red curve in Fig. 3.4a exhibits the best fitting, which resembles the simulation result.

Figure 3.5a shows the two-dimensional map of λ with respect to w and h. It can be observed from the figure that a rotational symmetry was present in the two-dimensional map as shown by the dashed circular arcs. This rotational symmetry can be used to develop an empirical relation $\lambda = \alpha\sqrt{w^2 + h^2}$. The values of λ were plotted with respect to $\sqrt{w^2 + h^2}$ to determine the validity of the empirical relation as shown in Fig.3.5b. The blue and green curves represent the simulation and analytical results, respectively. It can be observed that the data points converged on the single proportionality shown by the red line. From the best fitting of the linear proportionality, the slope α was determined as 0.39. The purple symbols represent the experimental measurement results, which verified the validity of the present empirical relation.

An empirical relation can be constructed between V_{AH} and x_{DW} using the abovementioned observations, which can be written as:

$$x_{\mathrm{DW}} = \alpha\sqrt{w^2 + h^2}\tanh^{-1}(V_{\mathrm{AH}}) \text{ with } \alpha = 0.39. \tag{6}$$

This equation can be used to determine x_{DW} by measuring V_{AH} in the Hall bar geometry. Additionally, the empirical relation provides a simple equation for the electrical detection range of a magnetic domain wall.

a

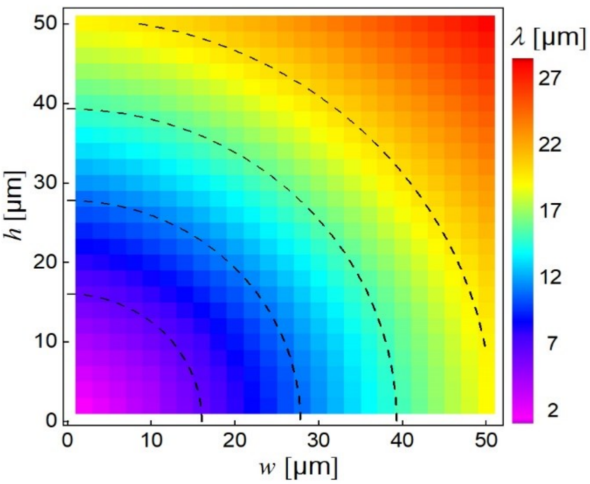

b

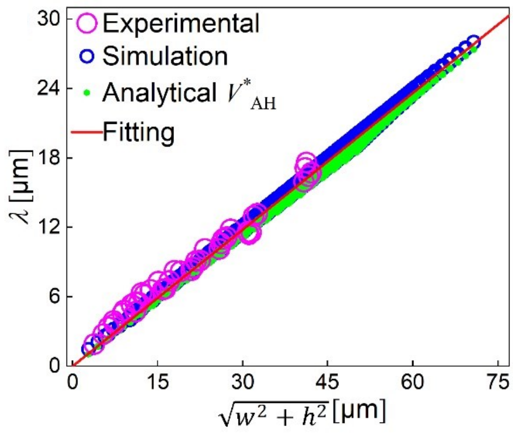

Figure 3.5 a, Two-dimensional map of λ with respect to w and h. The color corresponds to the value of λ as shown by the color palette on the right. The dashed circular arcs have their center at the origin, $(\lambda, w) = (0,0)$. **b,** Plot of λ with respect to $\sqrt{w^2 + h^2}$. The purple, blue, and green symbols represent the experimental, simulation, and analytical results, respectively. The red line represents the best linear fitting.

Chapter 3.6 Conclusion

In conclusion, the Hall voltage investigated in a Hall bar geometry as a function of position of DW using a numerical simulation, analytical equation, and experimental measurement. The results obtained using these methods results were identical to each other, which verified validity of the approach. Finally, a simple empirical relation was presented, which can be used to determine the DW position by measuring the Hall voltage in the Hall bar geometry. The results of this study can provide a method to obtain more precise quantitative information during magnetic DW experiments.

Chapter 4. Independent Control of Spin-Orbit Torque

Spin-orbit torque(SOT) is one of the origins which make possible to move magnetic DW via charge current. In the past, the mechanism of current induced DW motion was expected by spin-transfer torque mechanism [61,62] and experimentally confirmed [63,64]. However, new driving mechanism, SOT, can achieve more efficient CIDWM [41,65].

Chapter 4.1 Introduction

The core mechanism for efficient CIDWM is the SOT, which determines the magnitude of the spin-torque, and DMI [11,17-19,39,41], which enables the efficient transfer of the spin-orbit torque to the magnetic domain wall.

These two effects play a crucial role in determining the direction of CIDWM as well as the efficiency of CIDWM. If these two parameters can be controlled independently, it will be possible to more precisely control the DW. Therefore in this chapter we describes the research on how to control SOT independently of DMI.

Chapter 4.2 Sample Fabrication & Measurement

Metallic ferromagnetic thin films were fabricated on the Si 525 μm / SiO_2 100 nm substrate by use of DC magnetron sputtering with ultrahigh vacuum, which is 3×10^{-8} torr. Deposition environment with 2 mtorr Ar pressure was purged and maintained. Also 10 minutes of presputtering of materials was applied.

All of the fabricated samples show PMA and ,for the electrical measurement, they were made to micro wire structure with the process of photolithography, ion milling, and lift off, as shown in Fig 4.1. These samples were grouped into A and B. Because SOT and DMI share the same origin which is spin-orbit coupling, it is hard to control them independently. To find the clue to control the SOT, independent of DMI, sample group A mainly focuses on the material structure as shown in table 1. Sample group B mainly focuses on the thickness of material with the variation of upper Pt layer thickness (t) in Ta (5) / Pt (2.5) / Pd (0.3) / Co (0.4) / Pt (t), where the thickness range is from 1.0 nm to 4.0 nm with 0.5 nm increments and the number in parenthesis is in nanometer unit.

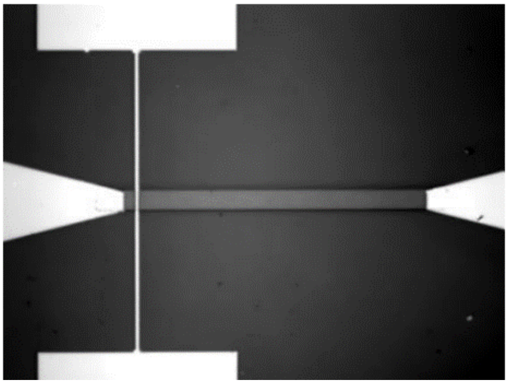

Figure 4. 1 Image of patterned micro wire structure with 350 μm length and 20 μm width.

Table 4. 1 Layer structures of sample group A

Sample	Structure
I	Ta (5.0) / Pd (2.0) / Co (0.5) / Pt (1.5)
II	Ta (5.0) / Au (2.5) / Co (0.5) / Pt (1.5)
III	Ta (1.5) / Pt (2.5) / Co (1.1) / Ta (2.5) / Pt (1.0)
IV	Ta (1.5) / Pt (2.5) / Co (1.0) / W (5.0) / Ta (2.0)
V	Ta (5.0) / Pt (2.5) / Pd (0.3) / Co (0.4) / Pt (1.0)

Chapter 4.3 Experimental result of H_{DMI} & $\varepsilon_{sat,SOT}$ in various magnetic trilayer structure

The maximum saturation SOT efficiency, $\varepsilon_{sat,SOT}$, and DMI-induced effective magnetic field, H_{DMI}, were measured through the measurement of depinning field of the DWs with respect to the in-plane magnetic field, H_x [24,37,38]. The procedure of measurement is as follows. With the application of negative z-direction magnetic field, single down domain state is made. Next, to make the up direction of magnetic domain, current pulse is applied to the writing line. With tens of μm away from the writing line, by increasing z-direction magnetic field with current bias, depinning field was measured with respect to the in-plane magnetic field. As shown in Table 2, sign of DMI and SOT was same for all the samples in group A except for the last sample structure. As a result, by changing material structure, we cannot control the SOT, independent of DMI. This is because SOT and DMI share the same origin which is spin-orbit coupling at the interface.

Table 4. 2 Measured values of H_{DMI} and $\varepsilon_{\mathrm{sat,SOT}}$ of sample group A

Sample	H_{DMI} [mT]	$\varepsilon_{\mathrm{sat,SOT}}$ [10^{-14} Tm^2/A]
I	150 ± 3	13.0 ± 0.1
II	132 ± 3	16.7 ± 2.6
III	-283 ± 8	-15.4 ± 0.4
IV	-293 ± 17	-14.3 ± 0.3
V	155 ± 12	-4.2 ± 0.1

However another sample group B shows, as in figure 4.3, that by increasing the thickness of upper Pt layer not only the modulus but also the sign of $\varepsilon_{\mathrm{sat,SOT}}$ was changed [31,37]. This is because one of the origins of SOT is spin Hall effect, which is bulk effect.

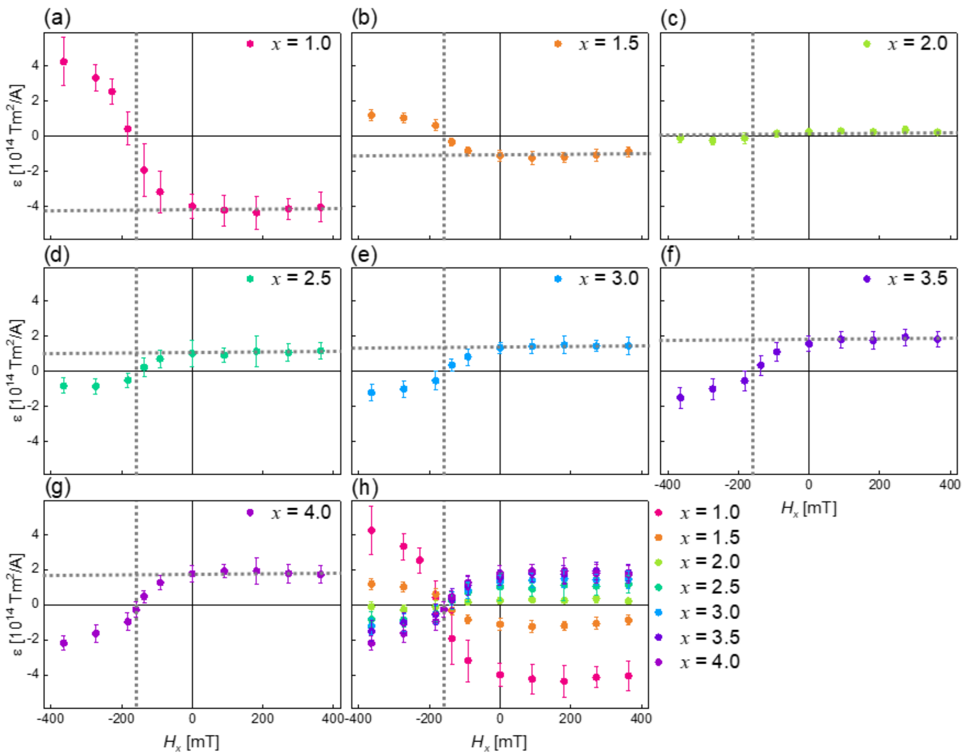

Figure 4.2 Spin-torque efficiency with respect to H_x in Ta (5) / Pt (2.5) / Pd (0.3) / Co (0.4) / Pt (x) where x = 1.0, (a), x = 1.5, (b), x = 2.0, (c), x = 2.5, (d), x = 3.0, (e), x = 3.5, (f), x = 4.0, (g), and all in one graph, (h). Intercept between abscissa and vertical gray dashed line shows $-\mathrm{H}_{\mathrm{DMI}}$ and intercept between ordinate and horizontal gray dashed line shows $\varepsilon_{\mathrm{sat,SOT}}$.

Chapter 4.4 Conclusion

In this chapter, here we show the strategy to control the SOT, independent of DMI. Because both two mechanisms originate from the spin-orbit coupling, by only changing the thickness of metal here we can only control the spin-orbit torque efficiency with respect to the thickness of Pt layer. Stemming from this result, this can be used to control the position of magnetic domain wall, via lateral asymmetric thickness control of Pt.

Chapter 5. Position Control of DWs via SOT Modulation in micro-structure

Racetrackmemory [50,51], which is attentioned by its efficiency, fast ratency, and capacity, is derived based on the current-induced domain wall motion. However, magnetic domain wall has intrinsic randomness about positionning, which can inboke malfunction of racetrack memory. This randomness was first reported by A. Yamaguchi et al., [66]. As shown in Fig 5.1, travel distance of magnetic domain wall is not constant with respect to the same injected current pulse. The stochacity of magnetic domain wall is due to the interaction between magnetic domain wall and the pinning sites, which is inevitable. To breakthrough the randomness of magnetic DW, diverse strategy was proposed and explored, including notch [50], metal diffusion [67], staggered geometry [68-70], and so on [71,72].

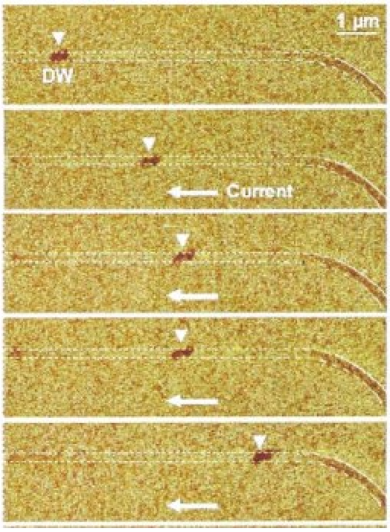

Figure 5. 1 MFM images with respect to current pulses [66].

Chapter 5.1 Introduction

After the discovery of current-induced domain wall motion, diverse method to precisely control the position of magnetic domain wall was reported. That is because the DW shows stochastic behavior with respect to the same input current. To breakthrough this problem which can invoke malfunction for using magnetic domain as memory H.-S Whang [73] and S.-B Choe proposed how to pinned/depinned the DW at the precise position with simulation. Their first idea is using geometrical notch aligning with spin-orbit torque modulation boundary. Because geometrical notch makes device more volnerable to the electric current, their next trial focus on the notch-free operating device. Thus the second trial is using triangular shape of spin-orbit torque modulation boundary. However, this trial doesn't work without edge pinning. As a result, their final version of notch-free operating device is step-function shape of modulation boundary. In this chapter, based on the experimental result of chapter 4 and idea of H.-S. Whang and S.-B. Choe, here we show the experimental proof of principle in micro-sized device.

Chapter 5.2 Experimental Background

By use of ultrahigh vacuum DC magnetron sputtering chaber, here we fabricated the magnetic thin film which is Ta (5 nm) / Pt (2.5 nm) / Pd (0.3 nm) / Co (0.4 nm) / Pt (1.5 nm) from the sibstrate Si 525 μm / SiO_2 100 nm. For the application of electric current, process of photolithography, ion milling and lift off was conducted. By use of magneto-optical Kerr effect microscopy, here we observe the current-induced domain wall pinning/depinning process.

Chapter 5.2.1 Pinning mechanism at SOT-Modulation boundary

As can be seen from the result of chapter 4, here we can modulate the efficiency of spin-orbit torque by changin the thickness of Pt layer. Thus if we make the laterally asymmetric layer of Pt, we can control the direction of magnetic domain wall, which is the mechanism of pinning. With similar modulus of spin torque efficiency but reversed sign, magnetic domain wall inevitably stop at the spin-orbit torque modulation boundary, as shwon in Fig. 5.2.1.

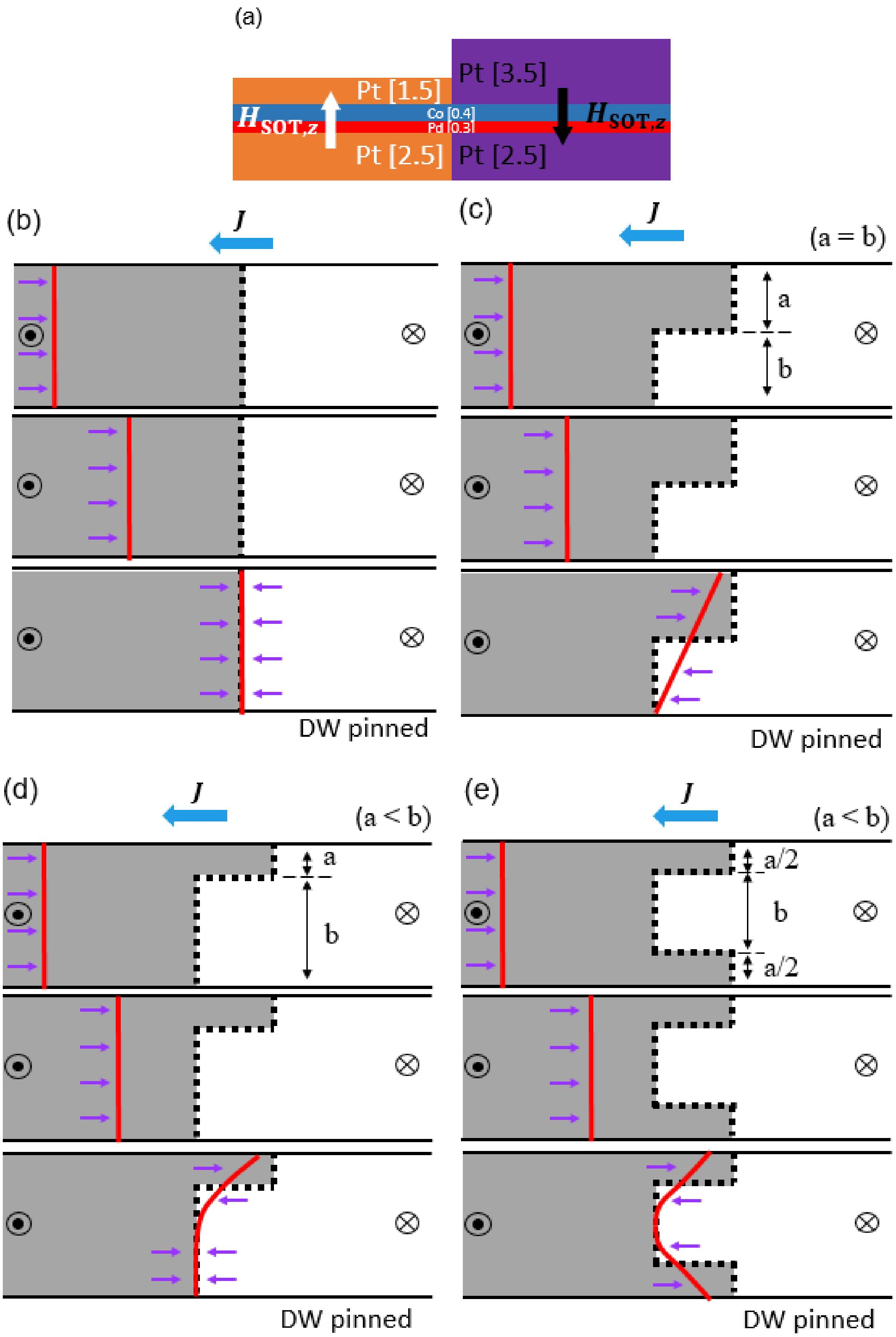

Figure 5. 1 Schematic illustration of domain wall pinning operating device structure from the cross view point. From the substrate, they share the same metal layers except for the upper

Pt layer. The orange colored Pt layer region exert spin-orbit torque with up direction to the domain wall which is white colored arrow with $H_{\mathrm{SOT,z}}$ and puple colored Pt layer region exert down directed spin-orbit torque to the domain wall which is black colored arrow. Number in the parentheses is in nanometer, (a). Schematic illustration of domain wall pinning process at the spin-orbit torque modulation boundary, where gray region shows upper Pt layer with 1.5 nm thickness and the white region shows upper Pt layer with 3.5 nm thickness, modulation boundary is illustrated as black dashed line, magnetic domain wall is illusrtated as red line which is the bounday between up direction with black circle left to the domain wall and down direction with black cross mark right to the domain wall, and purple arrow shows the direction of force being generated by spin-orbit torque, (b), (c), (d), and (e).

As proposed by H.-S. Whang et al., modulation boundary can be designed with diverse shap. Fig. 5.2.1. (b) shows the simplest design of modulation boundary which can stop the magnetic domain wall at the modulation boundary. However, one can make the shape of modulation boundary with step function to the transverse direction of the magnetic wire with the same step width, Fig. 5.2.1. (c), and different step width, Fig. 5.2.1. (d), and also for the double steps, Fig. 5.2.1. (e). In all of the designs, magnetic domain wall can not pass through the modulation boundary, because of the total summation of spin-orbit torque over the magnetic domain wall is zero at the boundary, which greatfully conduct the pinning operation.

Chapter 5.2.2 Depinning mechanism at SOT-Modulation boundary

As shortly mentioned at the introduction of this chapter, H.-S. Whang et al proposed the three kinds of strategy for the unidirection depinning at the spin-orbit torque modulation boundary. The common physical property of magnetic domain wall which is used for these strategies is tension of magnetic domain wall, which is one of the building block of magnetic domain wall energy. As magnetic domain wall energy is proportional to the total length of it, DW tends to minimize its length. As illustrated at the upper most of Figure 5.2.2. (a), (b), (c), let's consider the situation when we turn off the current after the magnetic domain wall stops at the step function shape modulation boundary, which is the final stage of Fig. 5.2.1. (c), (d), and (e).

With the charge current, due to the locally exerted but totally zero spin-orbit torque, magnetic domain wall was more lengthened than the length of magnetic domain wall without current. As the energy of magnetic domain wall is proportional to its length, if we turn off the current, magnetic domain wall will minimize its length at the modulation boundary, as can be seen in Fig. 5.2.2. (a), (b), and (c). From here, if we inject the reverse sign of charge current with respect to the current which is used at the pinning process, depending on the shpae of modulation boundary, magnetic domain wall can depin from the modulation boundary. Because of the same step width of modulation shape, as seen in Fig. 5.2.2. (a), magnetic domain wall cannot depin from the modulation. However, if we adopt the different width of steps as can be seen in Fig. 5. 2. 2. (b) and (c), as the total sum of spin-orbit torque to the domain wall is not zero. As a result here we can make the unidirectional depinning device.

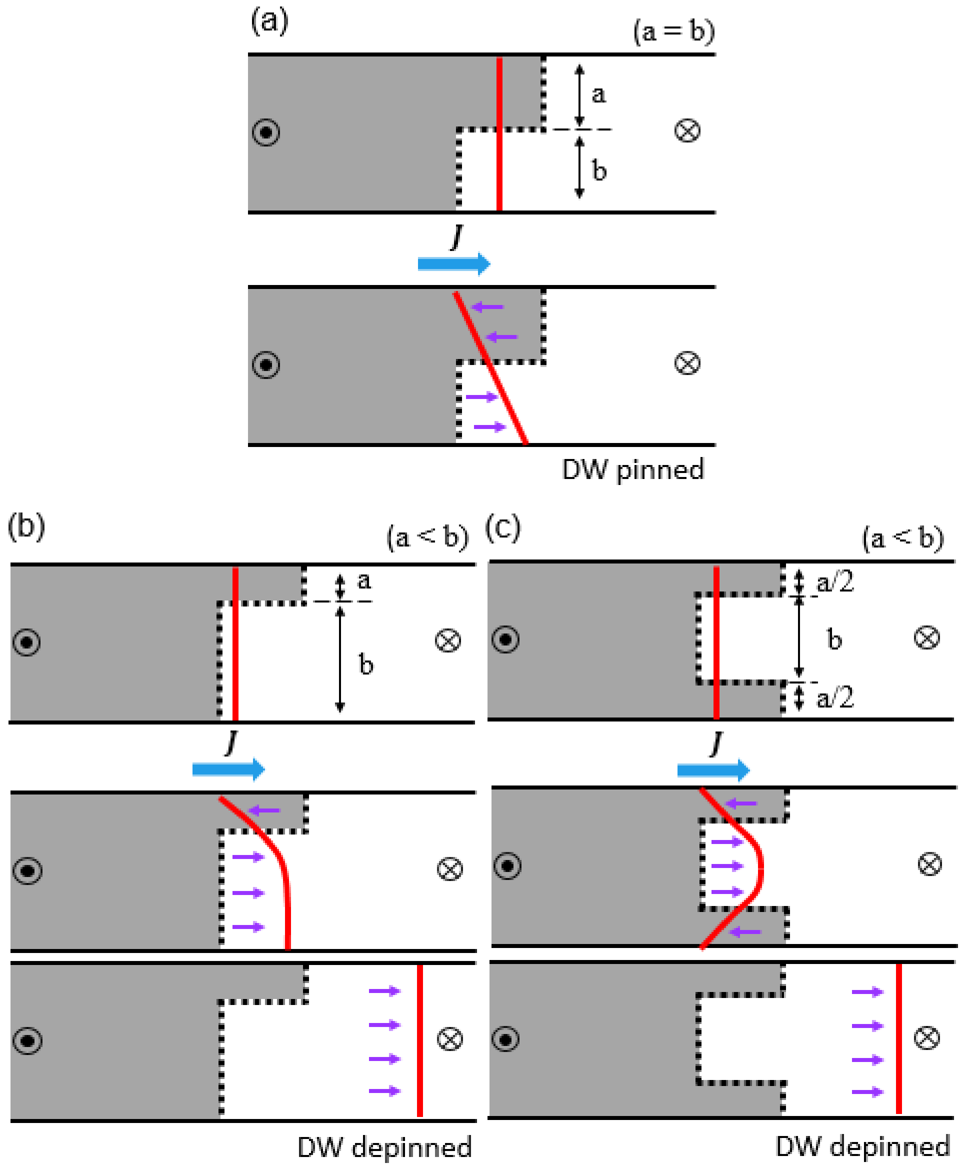

Figure.5.2. Schematic illustration of step function shape modulation boundary with same step width, (a), and different step width (b) and (c).

Chapter 5.3 Sample fabrication & Experimental Result

Based on the result of previous chapter, here we deposit the ultrathin metallic multilayer from the substrate (Si/SiO_2) Ta (5) / Pt (2.5) / Pd (0.3) / Co (0.4) / Pt (1.5) , number in the parenthesis is in nanometer, by use of ultra high vacuum ($\sim 3 \times 10^{-8}$ torr) DC magnetron sputtering chamber. The additional Pt layer with 2 nm thickness was lift off after the photolithography patterning process with step-function modulation shape and DC magnetron sputtering. With the process of photolithography, ion milling and lift off, unidirectional domain wall pinning/depinning device was fabricated.

Chapter 5.3.1 The simplest shape of SOT-Modulation boundary

As a first step, here we check that the magnetic domain wall is pinned at the modulation boundary by injecting charge current. By use of full-MOKE microscopy, pinning of magnetic domain wall at the modulation boundary was observed as can be seen at the Fig. 5.3.1. (a) and (b). As can be seen from this figure, regardless of initial position with respect to the modulation boundary, magnetic domain wall is positioned to the modulation boundary due to the reversed sign of spin-orbit torque.

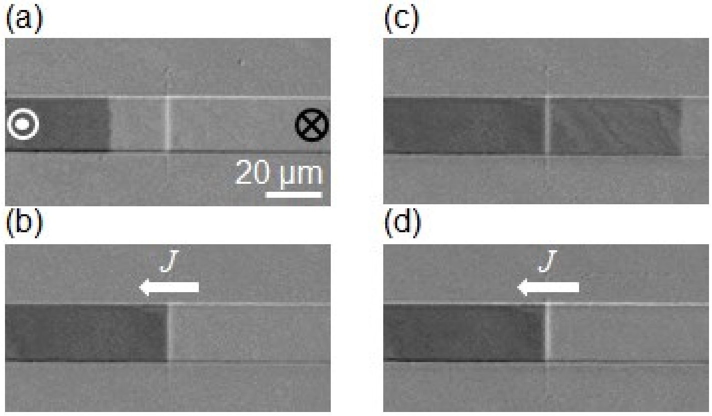

Figure. 5.3 Full-MOKE image of micro-patterned wire with modulation boundary which is position at the center of wire. Initial position of magnetic domain wall is left with respect to the modulation boundary. After injecting current pulse, magneitc domain wall positioned at the modulation boundary, (a). Initial position of magnetic domain wall is right with respect to the modulation boundary. For the same polarity of current pulse, magnetic DW positioned to the modulation boundary due to the reversed sign of spin-orbit torque. White bar is scale bar with 10 μm. Dark region shows up directed magnetic domain with white circle and the other region in the wire shows down directed magnetic domain with black cross mark.

Chapter 5.3.2 Analysis on single step-function shape of SOT-Modulation boundary

Now here we tried the design which is expected to be able to pin and depin the magnetic domain wall unidirectionally. Among the designs with different width of steps, we choose the multiple steps of modulation boundary shape as can be seen at Fig. 5.3.2. (a). Before we operate the series of modulation boundaries, here we investigate the probability of operation with respect to the diverse driving conditions of current pulses, where pulse with from 10 ms to 300 ms and pulse amplitude from 1.35 E+11 A/m^2 to 1.52 E+11 A/m^2 as in Figure. 5.3.2. (b), (c), (d), (e), (f), (g), (h), (i), (j), and (k). Each point of graph was calculated from the number of successful operation observed by full-MOKE over total number of try, which is 30. Also each graph was fitted with error function. For every measurement, magnetic domain wall was positioned via z-direction magnetic field, and the two series of current pulse was injected. The first current pulse is same for every measurement, because it is used to positioning magnetic domain wall to the boundary of modulation. The second current pulse was changed and injected for the statics of successful operation. Finally, the overall operating probability was plotted with 2-dimensional map as seen in Fig. 5.3.2. (l). As the experimental data clearly shows, in the case of same width of current pulse with different amplitude of current pulse, higher value of amplitude of pulse shows more successful result of operation.

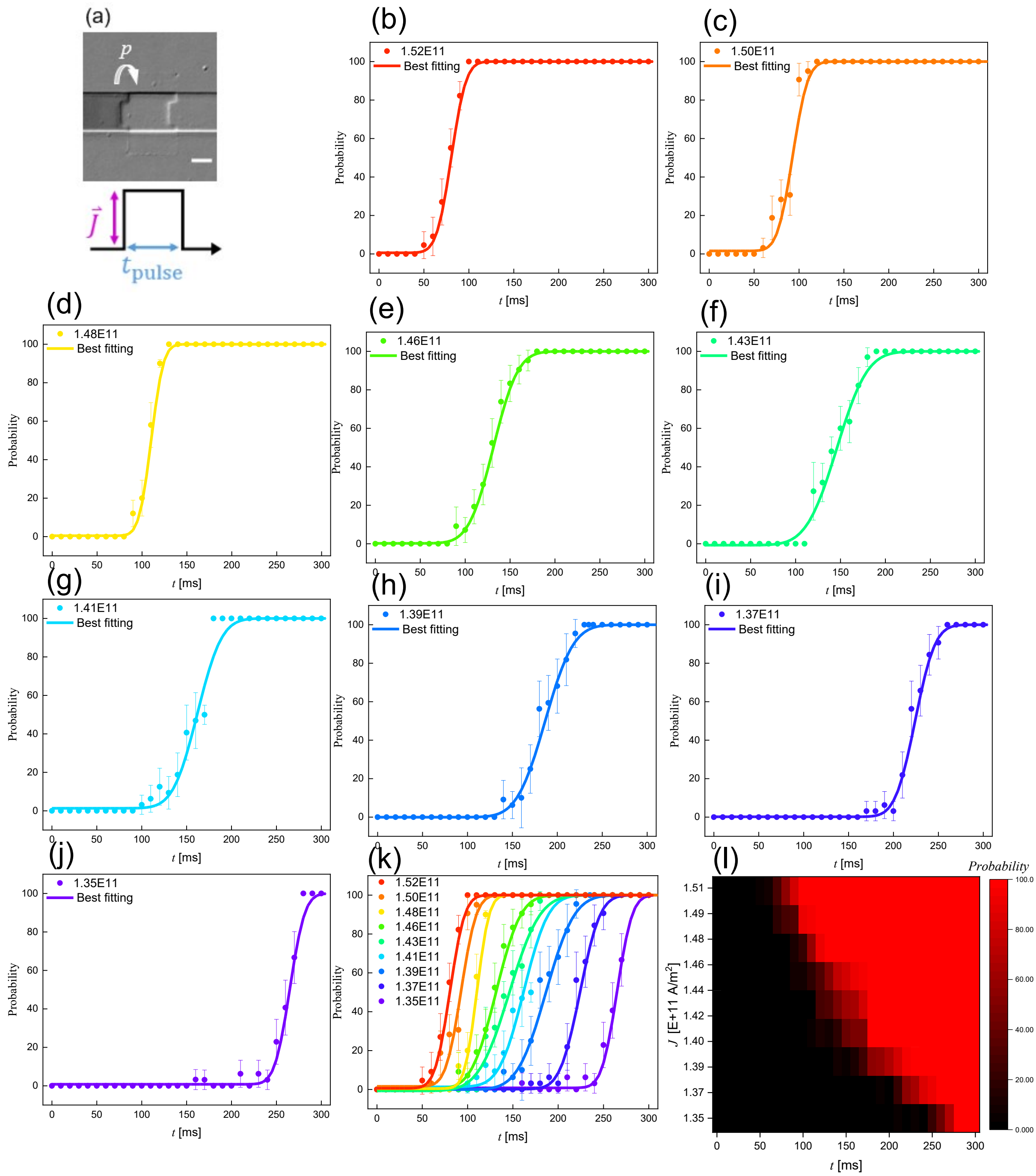

Figure. 5. 4. Full-MOKE image of multi step-function shape of spin-orbit torque modulation device, where the gray region, left to the modulation boundary, shows up directed magnetic domain, and the other region inside the wire shows down directed magentic domain. Probability of operation was calculated by changing the width and amplitude of current

pulses, (a). The ratio of number of successful operation, measured by full-MOKE, over total number of try, 30, was plotted from 10 ms to 300 ms with 10 ms increments with respect to the amplitude of current density 1.52, (b), 1.50, (c), 1.48, (d), 1.46 (e), 1.43, (f), 1.41, (g), 1.39, (h), 1.37, (i), 1.35, (j), E+11 A/m^2. Whole data was plotted in one graph, (k), and 2-dimensional map, (l).

Chapter 5.3.3 Operation of sequential array of SOT-Modulation boundaries

From the data of operating probability of single modulation boundary, here we describe the result of sequential array of spin-orbit torque modulation boundaries. As can be seen in Fig. 5.3.3 here we succeed to operate 12 number of modulation boundaries. Magneitc domain wall was initially positioned via z-direction magnetic field and, by injecting alternative sign of current pulses with 1.52 E+11 A/m^2 with 300 ms pulse width.

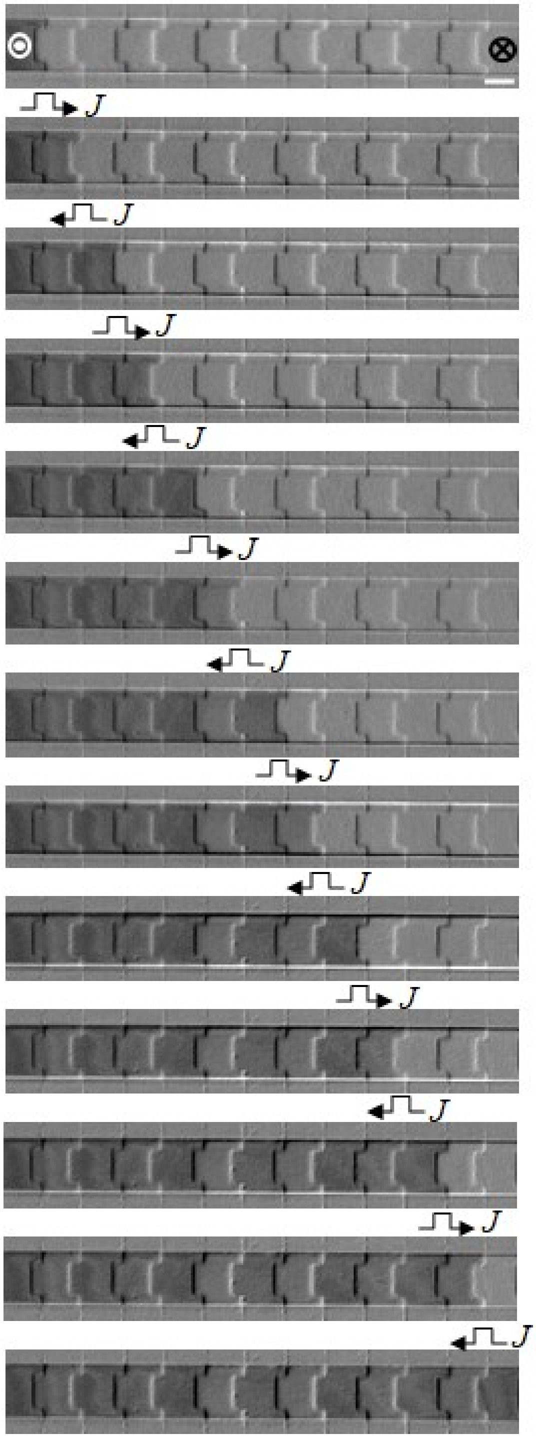

Figure 5.5 Sequential operation of spin-orbit torque modulation boundaries. For each image gray region with white circle shows up direction of magnetic domain and the other region inside the wire shows down direction of magnetic domain with black cross mark.

Chapter 5.4 Conclusion

In this chapter, here we provide new method to control the precise position of magnetic domain wall through spin-torque modulation boundary. Based on the simulation result for designing precise shape of modulation boundary and experimental result for reversing the sign of spin-torque efficiency, we confirm that the possibility for controlling precise position of magnetic DW in micro-sized mire. Because this method does not include any two dimensional geometric constraints, such as notch, more stability for current will be a merit. Though in this chapter only idea and micro-sized device is demonstrated, one can possibly think that also in nano-sized wire there is no reason that this idea not to be applied. By adopting this idea, we hope that one can achieve the shortest distance control of DW position in the world.

Chapter 6. Realization of Precise Control of DW Position in nano-structure

Control of magnetic DW via charge current motivate many researchers. As the HDD face the density limit of memory by superparamagnetic effect and also face the limit of process speed for using rotating disk, next generation memories continuously proposed. Magnetic memory based on DW was proposed but abandoned at one time. Because this 'bubble memory' operate via rotating magnetic field, which is demerit for miniaturazation. However, after the discovery of current induced-domain wall motion, this DW based memory shed new light as a next generation memory. Since the proposal by S. S. Parkin *et al*. [50], intense research about DW was studied, which result in the new driving mechanism at a diverse magnetic system [51].

Chapter 6.1 Introduction

Systematic and precise control of magnetic domain wall via spin-orbit torque modulation has never been tried. The current control limit of magnetic domain wall through charge current is about 1 μm. Because precise control of magnetic domain wall via charge current is paramount for realizing racetrack memory, diverse strategy has been tried to overcome the random behavior of magnetic domain wall. One example is geometric notch [50,74-76]. However, wire with notch structure is vernerable to the current due to the current bottle neck. Also notch increase the resistance of magnetic wire. By use of our new method to control the position of magnetic domain wall, here we show that without notch we can control the magnetic domain wall with the spatial resolution of 250 nm.

Chapter 6.2 Sample fabrication

To fabricate nanoscale device, we use electron-beam lithography process which was not treated in chapter 2. As a first step, one need to start the fabrication process with fabricating align mark. However, process of fabricating align mark don't need to be the first process. One also can make align mark, after deposition of magnetic thin film on the substrate. Process of making align mark is same with making electrode, different only for the shape and use of it. In addition, as e-beam lithography detect the align mark with its secondary electron, one needs to deposit enough thickness of Au. Here we deposit 150 nm of Au on the 5 nm of Ti buffer layer for adhesion between substrate and Au layer. Then by using DC magnetron sputtering, here we can deposit magnetic multilayer from the 2 inch silicon substrate with align mark (Si/SiO_2) Ta (5 nm) / Pt (2.5 nm) / Pd (0.3 nm) / Co (0.4 nm) / Pt (1.5 nm). From now on one can make the pattern of spin-torque modulation boundary with positive-tone of e-beam resist or negative-tone of e-beam resist. In practice, there should not be any difference but only for the sequence of spin-orbit torque modulation boundaries even we feel that using negative-tone of e-beam resist is more effectively change sign of spin-orbit torque of additionally deposited spin-orbit torque modulation region. Regardless of tone of e-beam resist, after lift off process of the 2 nm thickness of Pt layer, one can observe that the modulation structure was formed on the magnetic multilayer. Here we use ZEP-520A with dilluted to 25 % for the positive-tone e-beam resist and ma-N 2403 for the negative-tone e-beam resist. ZEP-520A with dilluted to 25 % was spin coated with 4000 rpm about 40 s and then baking at 90 degrees with 5 minute on the lift-off layer, which is LOR1A with dilluted 25 % and spin coated with 4000 rpm about 40 s with the baking at 90 degrees with 5 minute. For the negative-tone of e-beam resist, ma-N 2430, it is spin coated with 3000 rpm with 30 s and then, baked at 90 degrees with 60 s. After the spin coating and baking of e-beam resist, one needs to exposure electron beam on the resist.

Here we use JBX-9300 (jeol. Co at Korea Advanced Nano fab Center), which has 100 kV of acceleration voltage with 20 nm size of electron beam. By changing the exposure dose of electron beam with fixed time of develop, here we can find the optimal condition for nano patterning, which can fabricate 100 nm width of nanowire. After the process of exposure, positive tone of e-beam resist was developed by ZED-N50 with 80 seconds and negative tone of e-beam resist was developed by ma-D 525 with 76 seconds. After the process of lift off of 2 nm thickness of Pt layer, one can make pattern of nanowire align with the modulation boundaries. Here we use the negative-tone of e-beam resist, ma-N 2403 to pattern the nanowire. The following processes are ion milling and lift to make electrode (Fig 6.1).

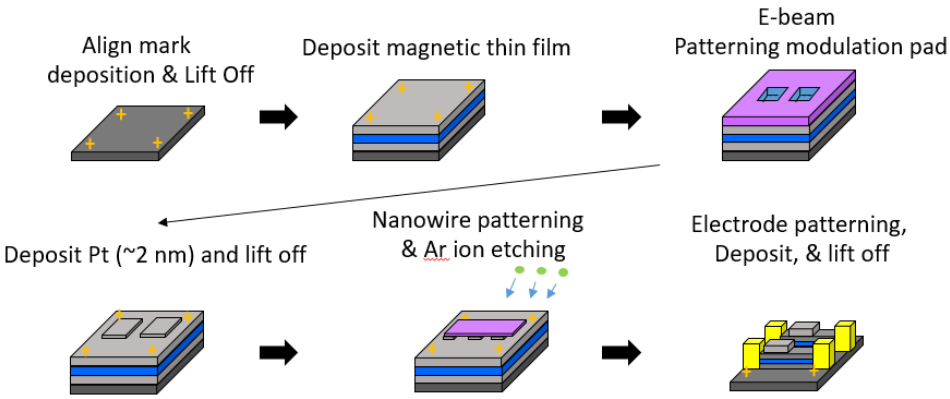

Figure 6. 1. Fabrication process of nano-sized spin-orbit torque modulated device

Chapter 6.3 Experimental result

As a first step, here we check that the additional Pt layer well reversed the sign of spin-orbit torque with similar value with respect to the other area. Confirmation of reversed spin-orbit torque was done at the micro patterned wire by e-beamlitho graphy, which is made at the same wafer. Also micro patterned structure of modulation boundary was tested and we confirm the successful operation. Then the last work is to measure the nano-sized modulation boundaries.

Due to the 250 nm period of spin-orbit torque modulation boundaries, here we measure the operation of modulation boundaries by use of scanning P-MOKE. Beam size of scanning P-MOKE is 2 μm, which can include 8 number of modulation boundaries. Experimental setup is shown as in Fig. 6. 2 (a). First, a large down direction of magnetic field was applied to saturate the magnetization into down direction. Then by applying current pulse from FG 1 to ground, DW was created at the right side of vertical yellow writing line. By scanning the surface of nano-wire, position of modulation was found. Then, by injecting current pulse, magnetic domain wall was initiated at the front of the modulation boundaries. Fig. 6. 2. (b) shows the nano-structure of the spot we measure. Finally, up side of Fig. 6. 2. (c) shows the measured current pulses with respect to time. The sequence of current pulses has same amplitude but alternative sign to unidirectionally drive the magnetic DW. Down side of Fig 6.2. (c) shows the MOKE signal of measuring spot with respect to the time, which is spontaneously measured with the current pulses.

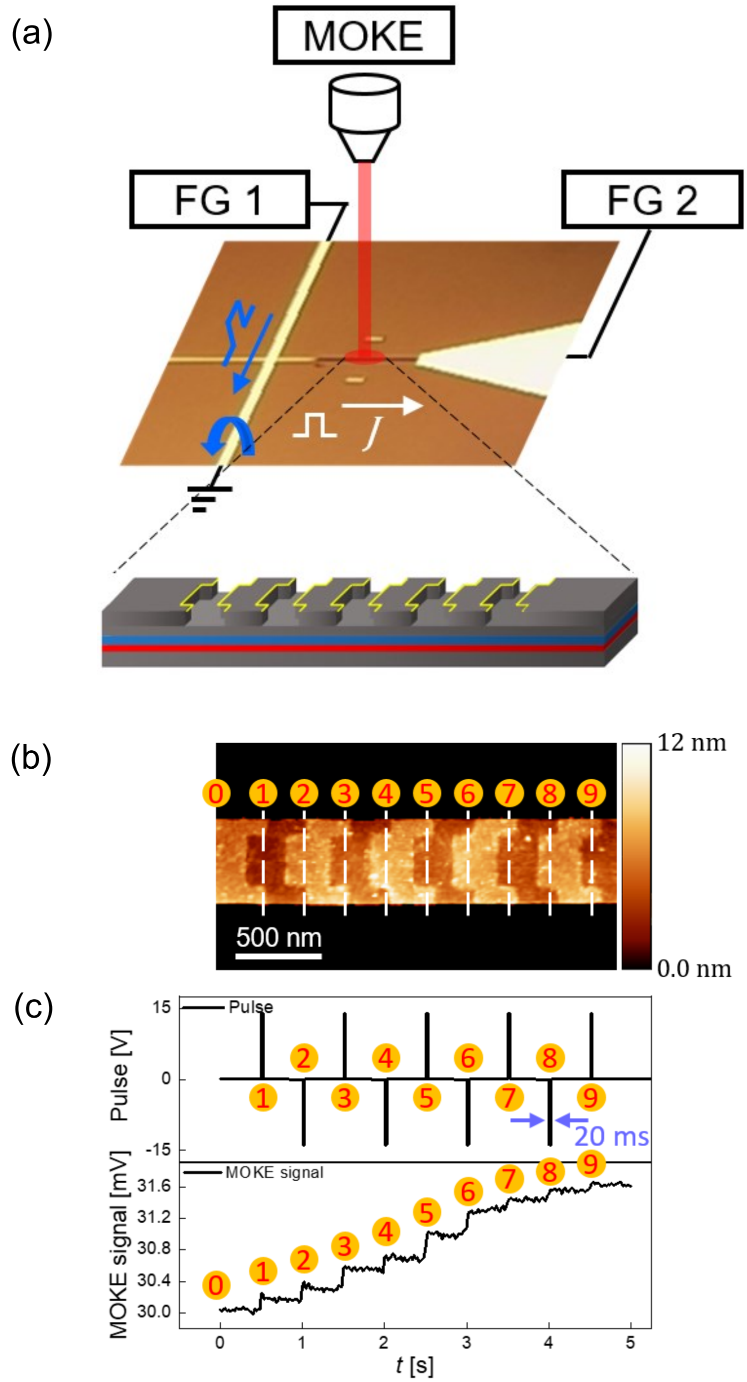

Figure 6. 2. Schematic illustration of experimental setup. By injecting current pulse from FG 1 to ground, one can write magnetic domain wall adjacent to the writing line. Then, through the current induced domain wall motion, magnetic domain wall is initiated to the front of modulation boundaries. Within the 2 μm beam size, structures of modulation

boundaries are illustrated at the down side (a). Atomic force microscopy image of measuring spot of scanning MOKE. The brighter (darker) the intensity, the higher (lower) the thickness (b). Result of simultaneous measurement of injecting current pulses and MOKE signal with respect to the time. Alternating sign of current pulses with same amplitude was injected sequencially. Amplitude and width of pulse is 2.6×10^{11} $\mathrm{A/m^2}$ and 20 ms. (c). Corresponding position of magnetic domain wall was numbered in (b) and (c).

As one can see from the Fig. 6. 2. (b) and (c), DW was first positioned at the position “0” in the Fig 6. 2. (b) with the corresponding MOKE signal is shown at the down side of Fig. 6. 2. (c). With the injection of positive polarity of current pulse numbered as “1” in up side of Fig 6. 2. (c) MOKE signal shows simultaneous jump from “0” to “1” signal level which corresponds to the DW position at the “1”. With the total 9 number of alternating current pulses, magnetic domain wall successfully pass through the modulation boundaries.

As a final step, we measured the operation probability to confirm the validity of our experimental result. The same amplitude but alternating 8 number of current pulses was applied repeatably 30 times. Operation probability (P) was calculated from the ratio between the number of successful operations and total operating number. Then, by organizing the different width and amplitude of current pulse set, operation probability was calculated, Fig 6.3. (a). The two-dimensional map of operating probability is shown in Fig 6. 3. (b).

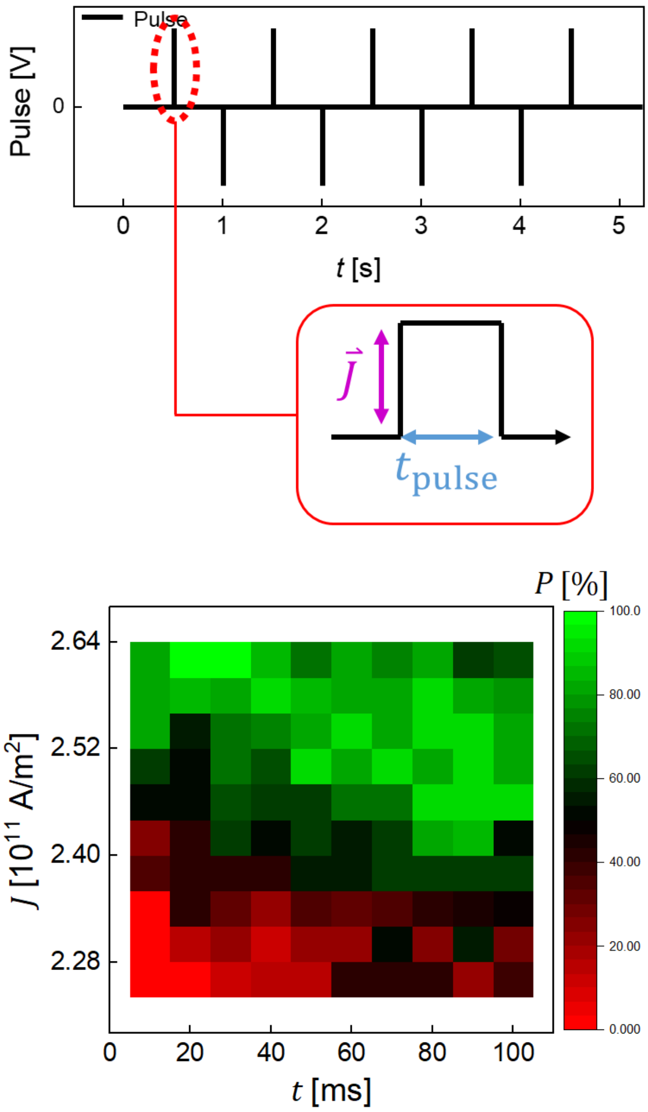

Figure 6. 3. Pulse sequence for measuring operation probability (a). Two-dimensional map of 8 number of serial operation probability (b). Each data point was calculated from the ration between the number of operation and total try number which is 30.

Chapter 6.4 Conclusion

In this chapter, we realize SOT-MB in nano-wire. Based on the result of changing SOT by regulating thickness of Pt layer and result of micro-wire structure, here we could realize series of controlled motion of DW down to the 250-nm. Another point of our strategy is that SOT-MB can prevent the tilting of DW which can invole the erasing of DW data bit. Two-dimensional map of probability of successful operation shows that specific amplitude and width of current pulses unidirectionally moves the DW easily. At the high amplitude and long width of current pulses, operating probability can be lowered by the thermal fluctuation. Not only for the efficiency of power consumption, but also for the successful operation short current pulses are recommended.

Chapter 7. Conclusion

Through this thesis, one can comprehend from the basic knowledge about properties of magnetic DWs to the state of art knowledge of DWs. As the conventional memory devices facing its limits in capacity, modern society of technology demand next-generation memory. One of the promising candidate is racetrack memory which move a series of DWs by charge current. However, there are problems in controlling DWs via charge current. Especially many researchers struggle with the randomness of DW positioning by charge current by means of notch, exchange biase and so on. However, in this thesis here we provide a new solution to precisely control the position of DW by SOT-MB. Although the idea looks simple, there was a lot of efforts to realize it to the nano-sized device. By use of SOT-MB, not only precise position of DW is possible down to the 250 nm, but also we can prevent the tilting of DWs. From the foundational control of SOT in micro-sized wire to the realization of nano-sized device, one can enjoy the whole procedure of experimental method and principle step by step at this thesis. We hope that this new strategy of controlling DWs provide a new breakthrough to realizing racetrack memory as next-generation memory device.

Reference

1. S. A. Wolf et al, Spintronics: a spin-based electronics vision for the future, Science 294 (5546), 1488-1495 (2001)
2. A. P. Malozemoff and J. C. Slonczewski Magnetic Domain Walls in Bubble Materials, Academic Press
3. R. C. O'Handley Modern Magnetic Materials: Principles and Application, Wiley
4. M. T. Johnson, P. J. H. Bloemen, F. J. A. den Broeder, and J. J. de Vries, Magnetic anisotropy in metallic mltilayers, Rep. Prog. Phys. 59, 1409-1458 (1996)
5. P. F. Carcia, A. D. Meinhaldt, and Suna, Perpendicular magnetic anisotropy in Pd/Co thin film layered structures
6. W. B. Zeper, F. J. A. M. Greidanus, P. F. Carcia and C. R. Fincher, Perpendicular magnetic anisotropy and magneto-optical Kerr effect of vapor-deposited Co/Pt-layered structures, J. Appl. Phys. 65, 4971 (1989)
7. F. J. A. den Broeder, D. Kuiper, A. P. van de Mosselaer, and W. Hoving, Perpendicular magnetic anisotropy of Co-Au Multilayers Induced by Interface Sharpening, Phys. Rev. Lett. 60, 26 (1988)
8. F. J. A. den Broeder, W. Hoving, and P. J. H. Bloemen, MAgnetic anisotropy of multilayers, J Magn. Magn. Mater, 93, 562-570 (1991)
9. S. Bandiera, R. C. Sousa, B. Rodmacq, and B. Dieny, Asymmetric interfacial perpendicular magnetic anisotropy in Pt/Co/Pt trilayers, IEEE Magn. Lett. 2, 3000504 (2011)
10. J. Ferre, J. P. Jamet, and P. Meyer, Magneto-Optical Studies of Magnetic

Ultrathin Film Structures, Phys. Stat. Sol. A 175, 213 (1999)

11. Y. -K. Park, Dzyaloshinskii-Moriya interaction in Pt / Co / NM trilayer system: beyond the interfacial perspective, Dissertation, Seoul National University, (2020)
12. N. Nagaosa, J. Sinova, S. Onoda, A. H. MacDonald, and N. P. Ong, Anomalous Hall effect, Rev. Mod. Phys. 82, 1539 (2010)
13. R. Karplus and J. M. Luttinger, Hall Effect in Ferromagnetics, Phys. Rev. 95, 1154 (1954).
14. J. Smit, The spontaneous Hall effect in ferromagnetics I, Physica, 21, 877 (1955).
15. L. Berger, Side-Jump Mechanism for the Hall Effect of Ferromagnets, Phys. Rev. B 2, 4559 (1970).
16. M. I. Dyakonov and A. V. Khaetskii, Spin Physics in Semiconductors, Springer 211-243.
17. I. Dzyaloshinsky, A thermodynamics theory of "weak" ferromagnetism of antiferromagnetics, J. Phys. Chem. Solid. 4, 241-255 (1958).
18. T. Moriya, Anisotropic superexchange interaction and wak ferromagneism, Phys. Rev. 120, 91-98 (1960).
19. A. Fert, and P. M. Levy, Role of anisotropic exchange interactions in determining the properties of spin-glasses, Phys. Rev. Lett. 44, 1538-1541 (1980).
20. A. Belabbes, G. Bihlmayer, F. Bechstedt, S. Blugel, and A. Manchon, Hund's Rule-Driven Dzyaloshinskii-Moriya Interaction at 3d-5d Interfaces, Phys. Rev. Lett. 117, 247202 (2016).
21. C. Moreau-Luchaire, C. Moutafis, N. Reyren, J. Sampaio, C. A. F. Vaz, N.

Van Horne, K. Bouzehouane, K. Garcia, C. Deranlot, P. Warnicke, P. Wohlhuter, J.-M. George, M. Weigand, J. Raabe, V. Cros, and A. Fert, Additive interfacial chiral interaction in multilayers for stabilization of small individual skyrmions at room temperature, Nat. Nanotech. 11, 444-448 (2016)

22. S.-G. Je, et al. Asymmetric magnetic domain-wall motion by Dzyaloshinskii-Moriya interaction, Phys. Rev. B 88, 214401 (2013).
23. D.-Y. Kim et al, Chirality-induced antisymmetry in domain-wall speed, NPG Asia Mater. 10, e464 (2018)
24. S.-G. Je et al. Emergence of hugh negative spin-transfer torque in atomically thin Co layers, Phys. Rev. Lett. 118, 167205 (2017).
25. K.-J. Kim, J.-C. Lee, S.-J. Yun, G.-H. Gim, K.-S. Lee, S.-B. Choe, and K.-H. Shin, Electric Control of Multiple Domain Walls in Pt/Co/Pt Nanotracks with Perpendicular Magnetic Anisotropy, Appl. Phys. Express 3, 083001 (2010)
26. A. Hoffmann, Spin Hall effects in metals, IEEE Trans. Magn. 49, 5172-5193 (2013).
27. J. Sinova, S. O. Valenzuela, J. Wunderlich, C. H. Back, and T. Jungwirth, Spin Hall effects, Rev. Mod. Phys. 87, 1213 (2015).
28. L. Liu, C.-F. Pai. H. W. Tseng, D. C. Ralph, and R. A. Buhrman, Spin-Torque Switching with the Giant Spin Hall Effect of Tantalum, Science, 336, 6081 (2012).
29. Y. K. Kato, R. C. Myers, A. C. Gossard, and D. D. Awschalom, Observation of the Spin Hall Effect in Semiconductors, Science, 306, 5703 (2004).
30. T. Wang, J. Q. Xiao, and X. Fan, Spin-Orbit Torques in Metallic Magnetic

Multilayers: Challenges and New Opportunities, Spin, 7 (03), 1740013 (2017).

31. P. P. J. Haazen et al. Domain wall depinning governed by the spin Hall effect, Nat. Mater. 12, 299-303 (2013).
32. P. M. Haney, H.-W. Lee, K.-J. Lee, A. Manchon, and M. D. Stiles, Current induced torques and interfacial spin-orbit coupling : Semiclassical modeling, Phys. Rev. B 87, 174411 (2013).
33. I. M. Miron, K. Garello, G. Gaudin, P.-J. Zermatten, M. V. Costache, S. Auffret, S. Bandiera, B. Rodmacq, A. Schuhl, and P. Gambardella, Nature (London) 476, 189 (2011).
34. T. A. Moore, I. M. Miron, G. Gaudin, C. Serret, S. Auffret, B. Rodmacq, A. Schuhl, S. Pizzini, J. Vogel, and M. Bonfim, High domain wall velocities induced by current in ultrathin Pt/Co/AlOx wires with perpendicular magnetic anisotropy, Appl. Phys. Lett. 93, 262504 (2008).
35. J. E. Hirsch, Spin Hall Effect, Phys. Rev. Lett. 83, 9 (1999).
36. J.-S. Kim, Y.-S. Nam, D.-Y. Kim, Y.-K. Park, M.-H. Park, and S.-B. Choe, Comparison between spin-orbit torques measured by domain-wall motions and harmonic measurements, AIP Adv. 8, 056009 (2018).
37. S. Emori, E. Martinez, K.-J. Lee, H.-W. Lee, U. Bauer, S.-M. Ahn, P. Agrawal, D. C. Bono, and G. S. D. Beach, Spin Hall torque magnetometry of Dzyaloshinskii domain walls, Phys. Rev. B 90, 184427 (2014).
38. J. H. Franken, M. H. Herps, H. J. M. Swagten, and B. Koopmans, Tunable chiral spin texture in magnetic domain-walls, Sci. Rep. 4, 5248 (2014).
39. A. Thiaville, S. Rohart, E. Jue, V. Cros, and A. Fert, Dynamics of Dzyaloshinskii domain walls in ultrathin magnetic films, Europhys. Lett.

100, 57002 (2012).

40. T. Nishimura, D.-Y. Kim, D.-H. Kim, Y.-s. Kim, Y.-K. Park, N.-H. Kim, Y. Shiota, C.-Y. You, B.-C. Min, S.-B. Choe, and T. Ono, Interfacial Dzyaloshinskii-Moriya interaction and dampinglike spin-orbit torque in $[Co/Gd/Pt]_N$ magnetic multilayers, Phys. Rev. B 103, 104409 (2021)
41. S. Emori, U. Bauer, S.-M. Ahn, E. Martinez, and G. S. D. Beach, Current-driven dynamics of chiral ferromagnetic domain walls, Nat. Mater. 12, 611-616 (2013).
42. K.-S. Ryu, L. Thomas, S.-H. Yang, and S. Parkin, Chiral spin torque at magnetic domain walls, Nat. Nanotech. 8, 527-533 (2013).
43. J. Moon, S.-H. Lee, K. Kim, J.-H. Park, J.-Y. Chang, J.-S. Yu, and S.-B. Choe, Method to Check Sample Reproducibility by Measuring Magnetic Domain Wall Motion in Perpendicular Magnetic Anisotropy Thin Films, J. Korea Magn. Society 31(5), 225-228 (2021)
44. D.-Y. Kim, M.-H. Park, Y.-K. Park, J.-S. Yu, J.-S. Kim, D.-H. Kim, B.-C. Min, and S.-B. Choe, Huge domain-wall speed variation with respect to ferromagnetic layer thickness in ferromagnetic $Pt/Co/TiO_2/Pt$ films. Appl. Phys. Lett. 112, 062406 (2018).
45. S. Lemerle, et al Domain wall creep in an Ising ultrathin magnetic film, Phys. Rev. Lett. 80, 849-852 (1998).
46. P. Chauve, T. Giamarchi, and P. Le Doussal, Creep and depinning in disordered media. Phys. Rev. B 62, 6241-6267 (2000).
47. P. J. Metaxas, et al, Creep and flow regimes of magnetic domain-wall motion in ultrathin Pt/Co/Pt films with perpendicular magnetic anisotropy, Phys. Rev. Lett. 99, 217208 (2007).

48. K.-J. Kim, et al, Interdimensional Universality of Dynamics interfaces, Nature (London) 458, 740-742 (2009).
49. D.-H. Kim et al, Maximizing domain-wall speed via magnetic anisotropy adjustment in Pt/Co/Pt films, Appl. Phys. Lett. 104, 142410 (2014).
50. S. S. P. Parkin, M. Hayashi, and L. Thomas, Magnetic domain-wall racetrack memory, Science 320, 190 (2008).
51. S. S. P. Parkin and S.-H. Yang, Memory on the racetrack, Nat. Nanotech. 10, 195-198 (2015)
52. J. H. Franken, H. J. M. Swagten, and B. Koopmans, Shift registers based on magnetic domain wall ratchets with perpendicular anisotropy, Nat. Nanotech. 7, 499-503 (2012).
53. A. J. Schellekens, A. van den Brink, J. H. Franken, H. J. M. swagten, and B. Koopmans, Electric-field control of domain wall motion in perpendicularly magnetized materials, Nat. Comm. 3, 847 (2012).
54. D. A. Allwood, G. Xiong, C. C. Faulkner, D. Atkinson, D. Petit, and R. P. Cowburn, Magentic Domain-Wall Logic, Science, 309, 1688 (2005).
55. Z. Luo, A. Hrabec, T. P. Dao, G. Sala, S. Finizio, J. Feng, S. Mayr, J. Raabe, P. Gambardella, and L. J. Heyderman, Current-driven magnetic domain-wall logic, Nature (London) 579, 214 (2020).
56. C. Kittel and L. Brewer, Introduction to solid state physics, Wiley
57. J. Kotzler and W. Gil, Anomalous Hall resistivity of cobalt films: Evidence for the intrinsic spin-orbit effect, Phys. Rev. B 72, 060412(R) (2005).
58. X. M. Cheng, S. Urazhdin, O. Tchernyshyov, C. L. Chien, V. I. Nikitenko, A. J. Shapiro, and R. D. Shull, Antisymmetric magnetoresistance in magnetic multilayers with perpendicular anisotropy, Phys. Rev. Lett. 94,

017203 (2005).

59. R. T. Bate, J. C. Bell, and A. C. Beer, Influence of magnetoconductivity discontinuities on galvanomagnetic effects in Indium Antimonide, J. Appl. Phys. 32, 806 (1961).

60. D. L. Partin, M. Karnezos, L. C. deMenezes, and L. Berger, Nonuniform current distribution in the neighborhood of a ferromagnetic domain wall in cobalt at 4.2 K, Appl. Phys. 45, 1852 (1973).

61. L. Berger, Exchange interaction between ferromagnetic domain wall and electric current in very thin metallic films, J. Appl. Phys. 55, 1954 (1984).

62. J. Slonczewski, Current-driven excitation of magnetic multilayers, J. Magn. Magn. Mater. 159, L1 (1996).

63. D. Chiba et al. Control of multiple magnetic domain walls by current in a Co/Ni nano-wire. Appl. Phys. Express 3, 073004 (2010).

64. T. Koyama et al. Observarion of the instrinsic pinning of a magnetic domain wall in a ferromagnetic nanowire, Nat. Mater. 10, 194 (2011).

65. I. M. Miron et al, Fast current-induced domain-wall motion controlled by the Rashba effect, Nat. Mater. 10, 1038 (2011).

66. A. Yamaguchi et al, Real-space observation of current-driven domain wall motion in submicron magnetic wires, Phys. Rev. Lett. 92, 7 (2004).

67. T. L. Jin et al, Tuning magnetic properties for domain wall pinning via localized metal diffusion, Sci. Rep. 7, 16208 (2017).

68. M. A. Bahri and R. Sbiaa, Geometrically pinned magnetic domain wall for multi-bit per cell storage memory, Sci. Rep. 6, 258590 (2016).

69. M. A. Bahri, B. Borie, T. L. Jin, R. Sbiaa, M. Klaui, and S. N. Piramanayagam, Staggered magnetic nanowire devices for effective

domain-wall pinning in racetrack memory, Phys. Rev. Applied 11, 024023 (2019).

70. M. Mohammed, S. A. Risi, T. L. Jin, J. Kosel, S. N. Piramanayagam, and R. Sbiaa, Controlled spin-torque driven domain wall motion using staggered magnetic wires, Appl. Phys. Lett. 116, 032402 (2020).
71. I. Polenciuc et al, Domain wall pinning for racetrack memory using exchange bias, Appl. Phys. Lett. 105, 162406 (2014).
72. D. M. Burn and D. Atkinson, Control of domain wall pinning by localised focused Ga^+ ion irradiation on Au capped NiFe nanowires, J. Appl. Phys. 116, 163901 (2014).
73. H. -S. Whang, Spin dynamics under spin Hall effect modulation: Skyrmion oscillator, Dissertation, Seoul National University, (2019).
74. Y. Gao et al, Depinning of domain walls in permalloy nanowires with asymmetric notches. Sci. Rep. 6, 32619 (2016).
75. L. K. Bogart et al, Dependence of domain wall pinning potential landscapes on domain wall chirality and pinning site geometry in planar nanowires. Phys. Rev. B, 79, 054414 (2009).
76. A. Himeno et al, Propagation of a magnetic domain wall in magnetic wires with asymmetric notches. J. Appl. Phys. 97, 066101 (2005)

Publication list

1. ***Seong-Hyub Lee***, Yune-Seok Nam, Myeonghoe Kim, Minhwan Kim, and Sug-Bong Choe, "Empirical relation between the Hall voltage and domain wall position in a Hall bar geometry" *Current Applied Physics,* **41**, 178-182 (2022).

2. ***Seong-Hyub Lee***, Myeonghoe Kim, Hyun-Seok Whang, Yune-Seok Nam, Jung-Hyun Park, Minhwan Kim, and Sug-Bong Choe, "Electrical manipulation of magnetic domain wall position via spin-orbit torque modulation" **In preparation** (2022).

3. Joon Moon, ***Seong-Hyub Lee***, Kitae Kim, Jung-Hyun Park, Jun-Young Chang, Ji-Sung Yu, and Sug-Bong Choe, "Method to Check Sample Reproducibility by Measuring Magnetic Domain Wall Motion in Perpendicular Magnetic Anisotropy Thin Films" *J. Kor. Mag. Soc.* **31**(5), 225-228 (2021).

4. Joon Moon, Jaesung Yoon, Kitae Kim, ***Seong-Hyub Lee***, Dae-Yun Kim, and Sug-Bong Choe, "Multiple Walker breakdowns in magnetic multilayers" *Sci. Rep.* **12,** 2307 (2022).

5. Yune-Seok Nam, Dae-Yune Kim, Yong-Keun Park, Ji-Sung Yu, ***Seong-Hyub Lee***, Duck-Ho Kim, Byoung-Chul Min, and Sug-Bong Choe, "Exchange-stiffness measurement scheme based on domain-wall chirality transition" *Appl. Phys. Lett.* **121**, 072403 (2022).

6. Kitae Kim, ***Seong-Hyub Lee***, Yooleemi Shin, Ji-Wan Kim, Jung-Hyun Park, Jun-Young Chang, and Sug-Bong Choe, "Experimental verification of Thiele equation for skyrmion Hall angle" *Sci. Rep.* **Under review** (2022).

7. Myeonghoe Kim, ***Seong-Hyub Lee***, Minhwan Kim, Kitae Kim, Jaesung Yoon, Jung-Hyun Park, and Sug-Bong Choe, "Experimental verification of domain-wall tilting induced by Dzyaloshinskii Moriya interaction in current-driven domain-wall motion" J. Magn. Magn. Mater. **563**, 169857 (2022).

8. Ji-Sung Yu, Dae-Yun Kim, Joon Moon, ***Seong-Hyub Lee***, Jun-Young Chang, Duck-Ho Kim, Byoung-Chul Min, and Sug-Bong Choe, "Chirality-dependent roughness of magnetic domain walls" *Appl. Phys. Lett.* **121**, 172403 (2022).

9. Seyyoung Jeon, ***Seong-Hyub Lee***, and Sug-Bong Choe, "Energy landscape study by telegraph noise of domain wall motion" Curr. Appl. Phys. **44**, 29-32 (2022).

10. Jaesung Yoon, ***Seong-Hyub Lee***, Minhwan Kim, Duck-Ho Kim and Sug-Bong Choe, "Measurement Technique of Magnetic Anisotropy Field on Patterned Magnetic Structures" J. Appl. Phys. Lett. **132,** 223903 (2022).

Abstract in Korean (국문 초록)

수직자기 이방성을 가진 강자성 금속 필름은 오랫동안 메모리 응용 기능에 있어 주목을 받아왔다. 높은 이방성 때문에 자기 도메인들이 열에 취약하지 않을뿐더러 자기 도메인 또한 더 많이 밀집될 수 있다. 얇은 박망 형태의 구조에서 수직 자기이방성은 나노미터 이하의 수준과 계면에 아주 민감한 특성을 가지고 있다. 결과적으로 이러한 박막을 제작하기 위해서는 불순물이 없는 환경과 두께의 정밀한 제어가 필요하다. 수직자기 이방성을 띠는 시료에서, 자구벽의 전기적인 신호에 대한 물리적인 메커니즘과, 차세대 메모리 응용을 위해서도 연구가 진행되어왔다. 특히 자구벽을 전류를 통해 감지하고 조절하는 것은 이진 상태인 자화의 방향을 읽고 전달하는데 있어 중요하다.

자구벽의 전기적 감지 메커니즘에 대해 비정상 홀 효과가 제안되었고 자화의 방향을 결정하는데 사용되었다. 자구벽의 전기적 제어에 대한 물리적 메커니즘에 대한 연구들은 자구벽을 효율적으로 제어하는데 중요한 파라미터들을 제안하였다. 그 중 하나는 자구벽을 전류로 움직이는 주요한 원천인 스핀-오빗 토크이다. 다른 하나는 자구벽을 카이럴한 닐월로 만들어주는 쟐로샨스키-모리야 상호작용이다. 스핀-오빗 커플링으로부터 기인하는 이러한 파라미터 들은 금속 다층시스템에서의 중금속이나,

중금속과 강자성 금속 계면에서 발생하게 된다. 그들의 메커니즘이 공유되기 때문에, 효율적인 전류 인가 자구벽을 구현하기 위해 두 파라미터를 독립적으로 제어하는 것이 어렵다.

이러한 파라미터를 어떻게 조절하는지 찾은 후에, 우리는 자구벽의 정확한 위치제어에 초점을 기울였다. 강자성 필름에 무작위로 존재하게 되는 피닝 사이트들 때문에, 자구벽은 외부에서 인가하는 전류에 대한 이동거리가 확률적으로 변하게 된다. 자구벽의 랜덤한 이동거리를 제어하기 위해서 2차원적인 지형적 제약조건을 포함해서 많은 연구들이 보고되었다. 그러나 지형적인 노치를 사용하는 것은 디바이스의 끄트머리에 데미지를 줄수 있고, 더 높은 전류 밀도를 필요로 하게 된다.

챕터 2는 강자성층의 두께를 모노레이어 이하의 두께 레솔루션으로 제어하기 위한 스퍼터링 시스템 셋업에 관해 설명한다. 실시간으로 증착된 두께를 확인하며 컴퓨터 기반으로 셔터 스위치를 제어하는 시스템이 설치되었다. 극 자기광 커 효과 현미경을 이용하여 우리는 증착된 필름에 존재하는 자구벽의 동역학적 특성을 비교하였으며, 이는 긴 시간동은 합리적인 재현성을 보여주었다.

챕터 3은 자구벽을 비정상 홀 효과를 통해 전기적으로 감지하는 것에 초점을 기울였다. 홀전압과 자구벽의 위치간의 경험적인 관계가 세가지 다른 방식의 분석을 통해 유도되었다. 첫번째로, 자구벽의 홀시그널이

홀바 바깥에서도 측정된다는 것을 관찰했다. 와이어 너비와 홀바너비의 다양한 조합을 가지고 자구벽의 전기적 감지 범위가 실험적으로 분석되었다. 그 다음으로 지형적인 파라미터들과 감지범위 간에 관계를 찾기 위해, 뉴메리컬한 시뮬레이션이 수행되었다. 마지막으로 우리는 우리 실험 상황에 적용하기 위해 분석적인 수식을 변형하였다. 이 세가지 다른 접근들의 일치와 함께 경험적인 관계가 제안되었다.

챕터 4는 자구벽의 전기적 제어에 관해 논의한다. 다양한 샘플 구조들에서부터 금속층의 두께 제어까지의 조사를 통해 우리는 스핀-오빗 토크를 제어하기 위한 전략을 제시하였다. 비록 스핀-오빗 토크를 제어하는 것이 삼중층의 구조를 바꿈으로써 제어하는 것은 어려웠지만, 오롯이 물질의 두께를 제어함으로써 스핀-오빗 토크를 제어하는 것이 가능했다. 이 방법을 통해 쟐로샨스키-모리야 상호작용의 유효한 필드가 어떤 명백한 변화를 주지 않고, 스핀-오빗 토크의 크기만을 제어함으로써 자구벽의 운동방향을 제어할 수 있었다.

챕터 5는 챕터 4의 결과에 기반해서 자구벽의 전기적 위치제어에 대해 연구를 진행하였다. 이전 챕터의 결과와 H.-S. Whang 의 아이디어의 혼합으로부터 우리는 자구벽을 스핀-오빗 토크 변조경계에 자구벽을 고정시키는 방법과 한쪽방향으로 자구벽을 이동시키는 방법을 제시하였다. 스핀-오빗 토크 변조 경계에서 자구벽의 디피닝은 극 자기광 커 효과 현미경을 이용해 관찰되었다. 스핀-오빗 토크 변조 경계에서의 자구벽

피닝을 확인한 후에 자구벽을 한쪽 방향으로 움직이도록 하기 위해 비대칭적인 변조 경계 디자인을 제작하였다.

챕터 6은 이러한 스핀−오빗 토크 변조 경계를 통해 자구벽의 정확한 위치제어를 수백 나노미터에 달하는 나노와이어를 만들어서 그 소자의 작동을 확인할 수 있었다.

Keyword : 수직자기이방성, 자구벽, 비정상 홀 효과, 스핀-오빗 토크, 잘로샨스키-모리야 상호작용, 스핀-오빗 토크 변조
Student number : 2017-21690